Nosetip Bluntness Effects on Transition at Hypersonic Speeds: Experimental and Numerical Analysis

Pedro Paredes,[*]
National Institute of Aerospace, Hampton, VA 23666, USA

Meelan M. Choudhari,[†]   Fei Li,[‡]
NASA Langley Research Center, Hampton, VA 23681, USA

Joseph S. Jewell,[§]   Roger L. Kimmel,[¶]
U.S. Air Force Research Laboratory, Wright-Patterson Air Force Base, OH 45433, USA

Eric C. Marineau,[‖]
AEDC White Oak, Silver Spring, MD 20903, USA

Guillaume Grossir[**]
von Karman Institute for Fluid Dynamics, B-1640 Rhode-St-Genèse, Belgium

The existing database of transition measurements in hypersonic ground facilities has established that the onset of boundary layer transition over a circular cone at zero angle of attack shifts downstream as the nosetip bluntness is increased with respect to a sharp cone. However, this trend is reversed at sufficiently large values of the nosetip Reynolds number, so that the transition onset location eventually moves upstream with a further increase in nosetip bluntness. This transition reversal phenomenon, which cannot be explained on the basis of linear stability theory, was the focus of a collaborative investigation under the NATO STO group AVT-240 on Hypersonic Boundary-Layer Transition Prediction. The current paper provides an overview of that effort, which included wind tunnel measurements in three different facilities and theoretical analysis related to modal and nonmodal amplification of boundary layer disturbances. Because neither first and second-mode waves nor entropy-layer instabilities are found to be substantially amplified to initiate transition at large bluntness values, transient (i.e., nonmodal) disturbance growth has been investigated as the potential basis for a physics-based model for the transition reversal phenomenon. Results of the transient growth analysis indicate that stationary disturbances that are initiated within the nosetip or in the vicinity of the juncture between the nosetip and the frustum can undergo relatively significant nonmodal

---

[*]Research Engineer, Computational AeroSciences Branch, NASA LaRC. AIAA Senior Member
[†]Research Scientist, Computational AeroSciences Branch. AIAA Associate Fellow
[‡]Research Scientist, Computational AeroSciences Branch.
[§]Research Scientist, (Spectral Energies, LLC), AFRL/RQHF. AIAA Senior Member
[¶]Principal Aerospace Engineer, AFRL/RQHF. AIAA Associate Fellow
[‖]Currently Program Officer for Hypersonics at the Office of Naval Research. AIAA Senior Member
[**]Post-doctoral Fellow, Aeronautics and Aerospace Department

amplification and that the maximum energy gain increases nonlinearly with the nose radius of the cone. This finding does not provide a definitive link between transient growth and the onset of transition, but it is qualitatively consistent with the experimental observations that frustum transition during the reversal regime was highly sensitive to wall roughness, and furthermore, was dominated by disturbances that originated near the nosetip. Furthermore, the present analysis shows significant nonmodal growth of traveling disturbances that peak within the entropy layer and could also play a role in the transition reversal phenomenon.

Nomenclature

E	=	total energy norm
F	=	disturbance frequency
G	=	energy gain
h_t	=	total enthalpy
h_ξ	=	streamwise metric factor
h_ζ	=	spanwise metric factor
J	=	objective function
K	=	kinetic energy norm
k	=	peak-to-valley roughness height
L	=	reference length
m	=	azimuthal wavenumber
M	=	Mach number
N	=	Logarithmic amplification factor
$\bar{\mathbf{q}}$	=	vector of base flow variables
$\tilde{\mathbf{q}}$	=	vector of perturbation variables
$\hat{\mathbf{q}}$	=	vector of amplitude variables
Re_{kk}	=	roughness-height Reynolds number
Re_∞	=	freestream unit Reynolds number
Re_{R_N}	=	Reynolds number based on nose radius
Re_{ξ_T}	=	transition Reynolds number based on freestream velocity and transition location
r_b	=	local radius of axisymmetric body at the axial station of interest
R_N	=	nose radius
T	=	temperature

T_w	=	wall temperature
$T_{w,ad}$	=	adiabatic wall temperature
(u, v, w)	=	streamwise, wall-normal, and spanwise velocity components
(x, y, z)	=	Cartesian coordinates
α	=	streamwise wavenumber
δ_h	=	boundary layer thickness
δ_S	=	entropy layer edge
κ	=	streamwise curvature
ω	=	disturbance angular frequency
ρ	=	density
(ξ, η, ζ)	=	streamwise, wall-normal, and spanwise coordinates
$\Delta\xi$	=	streamwise interval considered for optimal growth analysis
ΔS	=	entropy increment
ϕ	=	angular coordinate
θ	=	cone half-angle
$\mathbf{M}$	=	energy weight matrix

Superscripts

$*$	=	dimensional value
H	=	conjugate transpose

Subscript

∞	=	freestream value
0	=	initial position
1	=	final position
j	=	juncture location
T	=	transition location

Abbreviations

AFRL	=	Air Force Research Laboratory
AEDC	=	Arnold Engineering Development Complex
DNS	=	direct numerical simulation
DPLR	=	data parallel-line relaxation
FST	=	freestream turbulence
NS	=	Navier-Stokes

LIF   =   laser-induced fluorescence

PNS   =   parabolic Navier-Stokes equations

PSE   =   parabolized stability equations

I. Introduction

Laminar-turbulent transition of boundary-layer flows can have a strong impact on the performance of hypersonic vehicles because of its influence on the surface skin friction and aerodynamic heating. Therefore, the prediction and control of transition onset and the associated variation in aerothermodynamic parameters in high-speed flows is a key issue for optimizing the performance of the next-generation aerospace vehicles. Although many practical aerospace vehicles are blunt, the mechanisms that lead to boundary-layer instability and transition on blunt geometries are not well understood as yet. A detailed review of boundary layer transition over sharp and blunt cones in a hypersonic freestream is given by Schneider [1]. As described therein, both experimental and numerical studies have shown that the modal growth of Mack-mode instabilities (or, equivalently, the so called second-mode waves) is responsible for laminar-turbulent transition on sharp, axisymmetric cones at zero angle of attack. Studies have also shown that increased nosetip bluntness has a stabilizing effect on the amplification of Mack-mode instabilities, which is consistent with the observation that the onset of transition is displaced downstream as the nose bluntness is increased. However, while the boundary layer flow continues to become more stable with increasing nose bluntness, experiments indicate that the downstream movement in transition actually slows down and eventually reverses as the nose bluntness exceeds a certain critical range of values. The observed reversal in transition onset at large values of nose bluntness is contrary to the predictions of linear stability theory, and therefore, must be explained using a different paradigm. While no satisfactory explanation has been proposed as yet, one of the physical effects that have been suspected to cause this transition reversal is the role of surface roughness.

Earlier measurements related to the effect of nose bluntness on frustum transition over hypersonic blunt cones have been thoroughly documented by Stetson [2]. He concluded that the details of the nose tip flow played an important role in the transition reversal process, even though the onset of transition occurred significantly farther downstream over the frustum of the cone. Stetson [2] also observed that the measured transition locations within this regime were not easily reproducible across different runs. At a fixed set of freestream conditions, transition onset was found to vary across a wide range of frustum stations, and at times, the boundary layer flow remained laminar over the entire cone. Nonaxisymmetric transition patterns were observed even at zero angle of attack, and the measured length of the transition zone was much larger than that for cones with smaller values of nose bluntness. Finally, Stetson observed that frustum transition in the transition-reversal regime was highly sensitive to surface roughness in the nosetip region. For smaller nosetip bluntness prior to transition reversal, the surface finish on the nosetip (or the frustum) appeared to have

4

no effect on frustum transition. Polishing the blunt nosetip before the wind tunnel run for the large bluntness cones resulted in either higher frustum transition Reynolds numbers or a completely laminar flow over the model. Primarily on the basis of this last observation, Stetson speculated that frustum transition for large bluntness cones was dominated by disturbances originating near the nosetip. Therefore, roughness-induced transient growth appears to be a reasonable explanation for the transition-reversal phenomena in large bluntness cones at high speeds.

Historically, the term "bypass transition" has been used to identify transition paths that cannot be explained via modal amplification of small-amplitude disturbances [3]. Well-known examples of bypass transition include the transition due to high levels of freestream disturbances, as for example, in turbomachinery, or the subcritical transition observed in Poiseuille pipe flow experiments [4–6], transition due to distributed surface roughness on flat plates [7, 8] or cones [9], and subcritical transition observed on spherical forebodies [10–13]. Because of the strongly favorable pressure gradient over blunt bodies such as hemispherical nose tips and spherical segment capsules, the laminar boundary layer is highly stable; and hence, the observed onset of transition on such bodies has been known as the "blunt-body paradox". In recent years, the phenomenon of transient, nonmodal amplification of disturbance energy has emerged as a possible explanation for many cases of bypass transition. Mathematically, the transient, nonmodal growth is associated with the nonorthogonality of the eigenvectors corresponding to the linear disturbance equations. Physically, the main growth mechanism corresponds to the lift-up effect [14–16], which results from the conservation of horizontal momentum in the course of spanwise varying wall-normal displacement of the fluid particles. The actual growth in any given scenario is determined by the details of the external disturbance environment. However, an upper bound on the magnitude of energy gain via transient growth can be predicted by using the so-called optimal growth theory, which is typically formulated to maximize the disturbance growth across a specified interval of streamwise locations. Regardless of the flow Mach number [17, 18], the disturbances experiencing the highest magnitude of transient growth have been found to be stationary streaks that arise from initial perturbations in the form of streamwise vortices. Schmid & Henningson [19] and Schmid [20] provide a thorough review of the transient growth theory and the earlier results from the literature.

Reshotko & Tumin [21] were able to successfully correlate the transition data from several wind tunnel experiments involving subcritical, nose tip transition by using a semiempirical correlation derived from the optimal transient growth theory, which provides an upper bound on the magnitude of transient growth under suitable constraints. Reshotko & Tumin [21] extended the ideas from Anderson et al. [22], who had investigated subcritical transition in a flat plate boundary layer due to moderate to high levels of freestream turbulence (FST) and had derived a correlation based on the optimal growth of boundary layer disturbances generated by the FST. Based on the hypothesis that a similar disturbance growth could also be initiated by distributed surface roughness over hypersonic blunt forebodies, Reshotko & Tumin [21] were able to develop a semiempirical transition correlation by linking a critical disturbance amplitude required for the onset of transition with the roughness height parameter via a gain function based on the optimal growth framework. Even though the relevance of the linear, optimal disturbance growth concept to realistic, rough nose tips remains

to be established, their work provides the first physics-based model toward a potential resolution of the blunt-body paradox. Unlike other established models based on empirical curve fits that are valid for a specific subclass of datasets, Reshotko & Tumin's optimal-growth-based transition criterion has been able to provide a reasonable correlation with the measurements in various wind tunnel and ballistic range facilities and for a broad range of surface temperature ratios. In follow-on work, Paredes et al. [23, 24] have revised the Reshotko & Tumin correlation by including the effects of nonparallel basic state evolution, curvature terms, and the variation of both inflow and outflow locations for the transient growth interval. Their results indicate that application of a more thorough theoretical framework reveals certain new features of optimal growth characteristics that were not indicated by the parallel framework used in the previous correlation. However, despite these changes, the constants in the transition correlation remain close to their original values.

Not withstanding the questions related to the physical relevance of optimal growth theory, the successful correlation of much of the available data by the Reshotko & Tumin correlation raises the possibility that a similar framework could also correlate (or, perhaps, explain) the observations of transition reversal over blunt cones. That possibility was investigated during a collaborative efforts under the NATO STO group AVT-240 on Hypersonic Boundary-Layer Transition Prediction focused on the problem of blunt cone transition and the potential role of transient growth in the transition reversal phenomenon. While the problems of blunt-body paradox and transition reversal over blunt cones share a key similarity by way of transition onset in the absence of (significant) modal instability, they also exhibit two major differences. First, the onset of transition in the latter case is typically observed over the frustum of the cone, as opposed to the nose tip in the case of blunt body paradox. As such, the transient growth characteristics of blunt cone boundary layers are also expected to be different, and in fact, more complex than those over a blunt nose without any frustum. Besides investigating the transient growth features over blunt cones, the NATO group's effort also included wind tunnel measurements in both U.S. and Europe, and a preliminary study related to the effects of an azimuthally-periodic array of roughness elements located near the sonic location over the nose tip. The current paper provides an overview of the collaborative work including both theoretical analysis and experimental measurements. The layout of the paper is as follows. First, experimental transition measurements over blunt cones at hypersonic freestream speeds from the literature are summarized and compared in Section II. In Section III, we apply the transient growth analysis to hypersonic blunt cones for selected flow conditions that match the experimental studies relevant to the NATO effort [2, 25]. Those results were used to determine the azimuthal spacing between roughness elements for the experimental measurements of roughness effects within the transition reversal regime. Section IV outlines the preliminary findings from that experiment, while the summary and conclusions are presented in Section V.

II. Overview of Transition Measurements over Blunt Cones

The effect of nosetip bluntness on boundary-layer transition is often assessed by plotting the transition Reynolds number as a function of the nosetip radius Reynolds number where both Reynolds numbers are based on the freestream conditions. Figure 1(a) presents the Reynolds number at the start of transition (Re_{ξ_T}) as a function of the nosetip Reynolds number (Re_{R_N}) for the experiments by Stetson [2] in the Air Force Research Laboratory (AFRL) Mach 6 high-Reynolds-number facility with R_N = sharp (A1), 0.5 (A2), 1.0 (A3), 1.5 (A4), 2.0 (A5), 2.5 (A6), 5.1 (A7), 7.6 (A8), 10.2 (A9), 12.7 (A10), and 15.2 mm (A11) cones; and by Aleksandrova et al. [26] in the Central Aerohydrodynamic Institute (TsAGI) UT-1M Ludwieg tube with with R_N = 0.5 (B1), 1 (B2), 2 (B3), 3 (B4), 4 (B5), 5 (B6), 6 (B7), 7 (B8), 8 (B9), 10 (B10), 12 (B11), and 14 mm (B12) cones. Both data sets are at a nominal freestream Mach number of 6 on straight 8° half-angle cones. The data from Stetson displays two distinct regions referred to as "small bluntness" where the transition location moves downstream with increased bluntness, and "large bluntness" where the transition location rapidly moves upstream. The data from Aleksandrova et al. [26] (indicated by star symbols) has a positive slope (small bluntness behavior) up to a critical Re_{R_N} of 1.3×10^5. Beyond this critical value, the transition appears to depend on uncontrolled disturbances due to nosetip roughness. In the critical region, groups of points clustered by nosetip radii of 3, 4, 5, 12, and 14 mm exhibit a decrease in the transition Reynolds number with an increasing nosetip Reynolds number, which is indicative of transition reversal. With the exception of the sharp and the 0.5 mm nosetips that consist of steel inserts, the cone model and nosetip inserts were made of AG-4 composite material. The roughness height of the AG-4 material was not specified by the authors, but is expected to be rougher than polished steel. The shape of the transition front, which was quantified using temperature-sensitive paint, revealed turbulent wedges at Reynolds numbers above the critical value. The authors attribute the formation of such wedges to the presence of uncontrolled nosetip roughness. The experiments from Aleksandrova et al. [26] illustrate that surface roughness has a significant effect on the emergence of the transition reversal. In Stetson's Mach 6 experiments [2], the nominal model surface finish had a root-mean-square (rms) value of 15 μin. (0.38 μm) and blunt nosetips were polished before each run. The polished nosetips most likely explain why the small bluntness behavior was extended to nosetip Reynolds numbers slightly above 9.0×10^5 in Stetson's experiments. The sensitivity of frustum transition to roughness at high nosetip Reynolds numbers was investigated by Stetson by adding $45 - 50$ μin. ($1.14 - 1.27$ μm) rms roughness on the 0.6 in. (15.2 mm) nosetip. The added roughness caused early frustum transition.

Figure 1(b) presents the Reynolds number at the start of transition as a function of the nosetip Reynolds number for three sets of experiments at nominal freestream Mach numbers between 9 and 10 on straight slender cones. The plot includes the experiments of Stetson [2] in Tunnel F at Mach 9 on 7° half-angle cones with R_N = sharp (C1), 1.5 (C2), 4.5 (C3), 7.5 (C4), 10.5 (C5), 14.0 (C6), 22.5 (C7), 55.4 (C8); of Marineau et al. [25] in Tunnel 9 at Mach 10 on 7° half-angle cones with R_N = 0.15 (D1), 5.1 (D2), 9.5 (D3), 12.7 (D4), 25.4 (D5), and 50.1 mm (D6); and that of Softley et al. [27, 28] in the G.E. shock tunnel on 5° half-angle cones with R_N = 0.25 (E1), 0.51 (E2), 1.3 (E3), 12.7
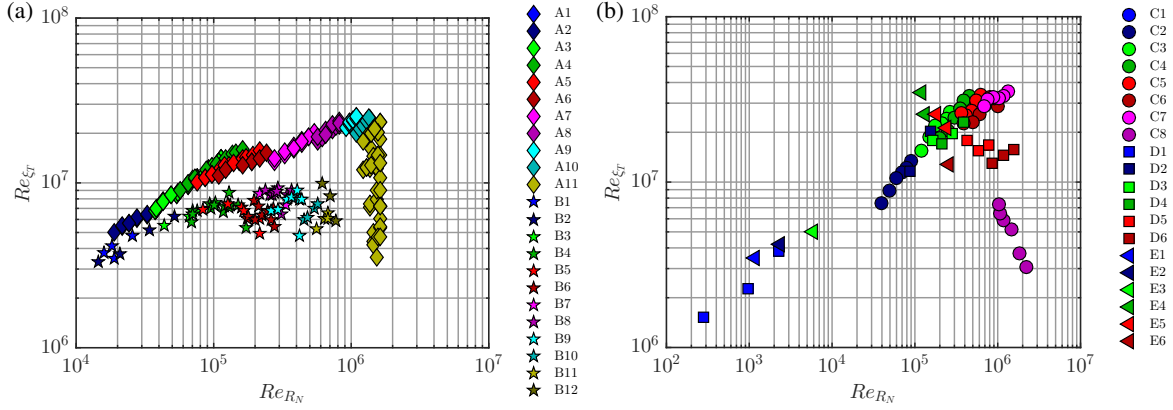
Fig. 1 **Transition Reynolds number based on freestream as a function of the nose Reynolds number at (a) Mach** **6 and (b) Mach** 9 **to** 10 **which illustrates the effect of bluntness and the transition reversal.**

(E4), 19.1 (E5), and 25.4 mm (E6). As seen at Mach 6, the Mach 10 data also displays the small bluntness and large bluntness regions. The boundary between the large bluntness and small bluntness occurs at varying Reynolds numbers of approximately 1.2×10^5, 3.9×10^5, and 9.0×10^5, respectively, for Softley, Marineau, and Stetson. The reason for the variation in the critical Reynolds numbers among the three data sets is not clear, since the respective experiments report similar surface finishes of 30, 32, and 40 μin. (0.76, 0.81, and 1.02 μm). Just like Stetson, Softley and Marineau also polished the nosetip prior to each run, but from the results it appears that the polished surface finish might have been smoother in Stetson's experiment.

As noted by Stetson [29], the use of "small bluntness" and "large bluntness" when discussing nosetip bluntness effects can be misleading, as the bluntness effect is related not only to the physical dimensions of the nosetip, but also to where transition occurs with respect to the nosetip. As discussed by Muir and Trujillo [30], the nosetip Reynolds number does not properly account for the various effects of the nosetip radius and unit Reynolds numbers. Stetson and Rushton [31] introduced the entropy-swallowing length as a parameter to relate the transition location to nosetip bluntness effects. Using Rotta's correlation [32], the entropy-swallowing length is found to be a function of $(Re_\infty)^{1/3}$ and $(R_N)^{4/3}$. One disadvantage of the entropy-swallowing length as a correlation parameter is that it cannot be easily defined for arbitrary geometries. Moreover, the blunt cone data is usually correlated by normalizing the transition locations (location or Reynolds numbers) on blunt cones by the transition length on sharp cones in order to remove unit Reynolds number effects. Such an approach cannot be extended to arbitrary geometries.

Boundary-layer stability calculations have tried to explain the transition behavior in hypersonic blunt cones. The effect of bluntness on the second-mode instability was first investigated by Malik et al. [33] and Herbert & Esfahanian [34] and more recently by Marineau et al. [25, 35] and Jewell and Kimmel [36]. These recent studies include parabolized stability equation (PSE) analysis of the historical Stetson Mach 6 and Mach 9 blunt cone experiments using the STABL software suite [37]. The stability analyses agree that the transition reversal cannot be predicted by only considering

8

Mack's second-mode instability mechanism. This is because increased bluntness stabilizes the second mode by moving the neutral point downstream due to local edge Mach number and local unit Reynolds number reductions within the entropy layer. This implies that the transition location based on Mack's second-mode amplification keeps moving downstream and eventually transition does not occur as the bluntness increases. In addition, the boundary-layer stability studies found that the first mode is also not destabilized by bluntness, so that it cannot be responsible for the transition reversal.

Even if transition reversal cannot be predicted with linear stability computations of the first and second modes, an approach combining the measurements and computations data will still be useful to evaluate where and when the transition process is no longer dominated by the second mode. Figure 2 presents a compilation of second-mode transition N-factors N_T as a function of the nosetip Reynolds number Re_{R_N} for the Mach 6 experiments of Stetson [2] from Ref. [36] (diamonds), Mach 9 experiments of Stetson [2] from Ref. [35] (circles) and Mach 10 experiments of Marineau et al. [25] (squares). For values of Re_{R_N} below 1×10^4, N_T increases with Re_{R_N} as a result of the increase in the unit Reynolds number. This behavior can be linked to an increase in the critical second-mode frequency f_T, which implies a lower tunnel noise content near f_T. This effect, first discussed by Marineau et al. [25] and Marineau [35], has recently been modeled by Balakumar and Chou [38] with direct numerical simulations (DNS) of the Tunnel 9 Mach 10 experiments. The approach includes the measured freestream noise spectrum and an empirical correlation (see Marineau et al. [25]) to determine the breakdown amplitude of the second mode. The sharp cone nosetip radius was not specified in either Stetson Mach 6 or Mach 9 experiments. To include these sharp cone data points in Fig. 2, the sharp nosetips were assumed to have the same radius as the sharp Tunnel 9 cone. A variation in the sharp cone nosetip radius does not change the trends, as it simply shifts the point left or right. For Re_{R_N} between approximately 4×10^4 and 1×10^5, a steep decrease in N_T with Re_{R_N} is observed. Somewhere in this region, the transition process appears to not be dominated by second-mode amplification. Note that the departure from second-mode-dominated transition occurs prior to transition reversal. The decrease of N_T with bluntness was discussed by Marineau [35] and attributed to a decrease of the second-mode breakdown amplitudes and to an increase in the initial amplitudes. The decrease in the breakdown amplitudes is linked to the lower edge Mach number whereas the increase in the initial amplitudes is related to the decrease in the critical second-mode frequency f_T as well as an increase in the receptivity coefficient with Re_{R_N}. For these conditions, the measured and estimated transition N-factors and the estimated receptivity coefficients are shown in Figs. 3(a) and 3(b), respectively.

In contrast to Stetson's blunt cone experiments, which measured just the transition location, Marineau et al. [25] also measured the boundary-layer instabilities by using a large number of high-frequency response pressure sensors (PCB®-132). These measurements captured the evolution of the pressure fluctuations over the surface of the cone. Figure 4 presents a map of the logarithm of the pressure power spectral density (log(PSD)) at $Re_\infty \approx 17 \times 10^6$ m^{-1} for $R_N = 0.15, 5.1, 9.5, 12.7, 25.4,$ and 50.8 mm. For $R_N \geq 5.1$ mm, the transition occurs before the entropy layer is
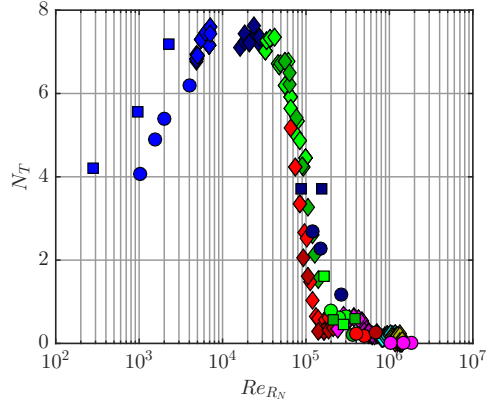
Fig. 2 Computed second-mode N-factors at the experimental transition location (start of transition) as a function of the nosetip Reynolds number. The same symbols and colors as in Fig. 1 are used to indicate the nosetip radius.
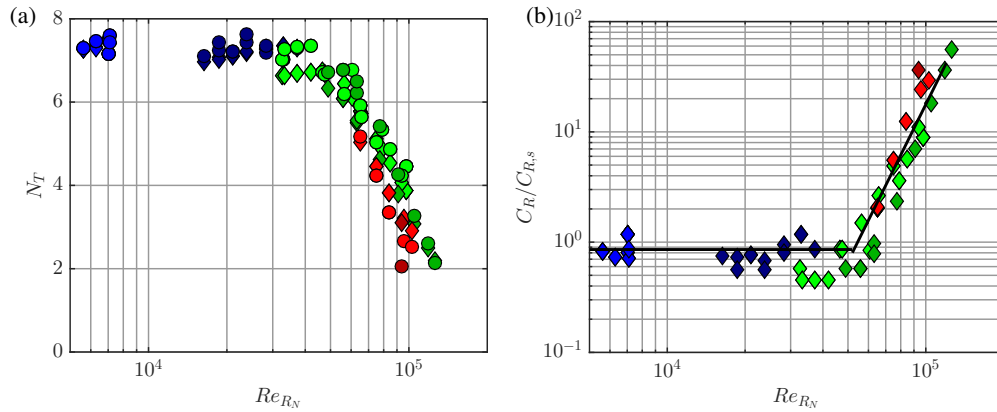

Fig. 3 Effect of bluntness on (a) transition N-factors and (b) receptivity for Stetson blunt cone experiments at Mach 6. The same symbols and colors as in Fig. 1 are used to indicate the nosetip radius.

swallowed. This leads to a significant reduction of the edge Mach number compared to the sharp cone case. For the 5.1 mm nosetip in Fig. 4(b), the edge Mach number varies from 4.4 to 4.8 between the neutral point and the start of transition. The bluntness significantly delays the appearance of the second-mode waves and increases the distances over which growth and breakdown occur. As a result of these two factors, the transition location is moved further downstream on the blunt cone (from 0.25 m on the sharp cone to 0.68 m on the 5.1 mm cone, based on heat transfer measurements). In addition, the second-mode frequencies are significantly lower on the blunt cone due to the increased boundary-layer thickness. As the nosetip radius increases from 5.1 mm to 9.5 mm, the transition location moves further downstream and the unstable second-mode frequencies are further decreased. The increase from 9.5 mm to 12.7 mm has a minor effect on the transition location, which indicates that reversal is near. For the 12.7 mm nosetip, the start of transition occurs prior to significant growth of the second mode. This indicates that transition was not initiated by the second-mode instability. However, further downstream within the transitional region, the second-mode amplitudes keep increasing up to the downstream end of the cone. The 25.4 and 50.8 mm nosetips are in the reversal regime as the transition location has moved upstream compared to those at the smaller radii. In addition, transition occurs before the appearance of second-mode waves. This makes sense, as the edge Mach number at the start of transition for the 25.4 mm and 50.8 mm radii are 3.3 and 3.2 respectively, which are too low for second-mode growth. The results for 25.4 mm and 50.8 mm nosetips also reveal that the mechanism responsible for the transition reversal has a weak pressure signature, as no significant variation in the pressure PSD is found.

The use of fast-response heat flux sensors can help to characterize the transition mechanisms on blunt cones. For instance, time-resolved heat transfer measurements performed at Mach 9 by Zanchetta [39] in the Imperial College Gun Tunnel on a 5° half-angle cone revealed that in the reversal regime, transitional events are formed in the near-nose region and convect downstream. The formation frequency of the events was linked to the severity of the roughness environment. In certain cases, second-mode instability waves and these transition events were occurring concurrently; and the experiments indicated that the second mode was responsible for the completion of transition. Recent laser-induced-fluorescence-based (LIF) schlieren measurements from Grossir et al. [40] on a blunt 7° half-angle cone at Mach 11.9 in the von Karman Institute Longshot hypersonic wind-tunnel revealed disturbances with shapes quite different from the usual second-mode rope structures. The disturbances that extend above the edge of the boundary layer are seen in Fig. 5 for the 4.75 mm nosetip radius. These disturbances, that were not present on schlieren images for sharper cones, could be a manifestation of the blunt cone transition mechanism leading to the heat transfer fluctuation measured by Zanchetta [39].

In summary, the experimental and numerical studies agree that frustum transition in the reversal regime cannot be accounted for via linear, modal instability analysis. Furthermore, the experimental observations agree that frustum transition on large bluntness cones is highly sensitive to wall roughness and appears to be dominated by disturbances that originate in the vicinity of the nosetip. Therefore, roughness-induced transient growth emerges as the primary
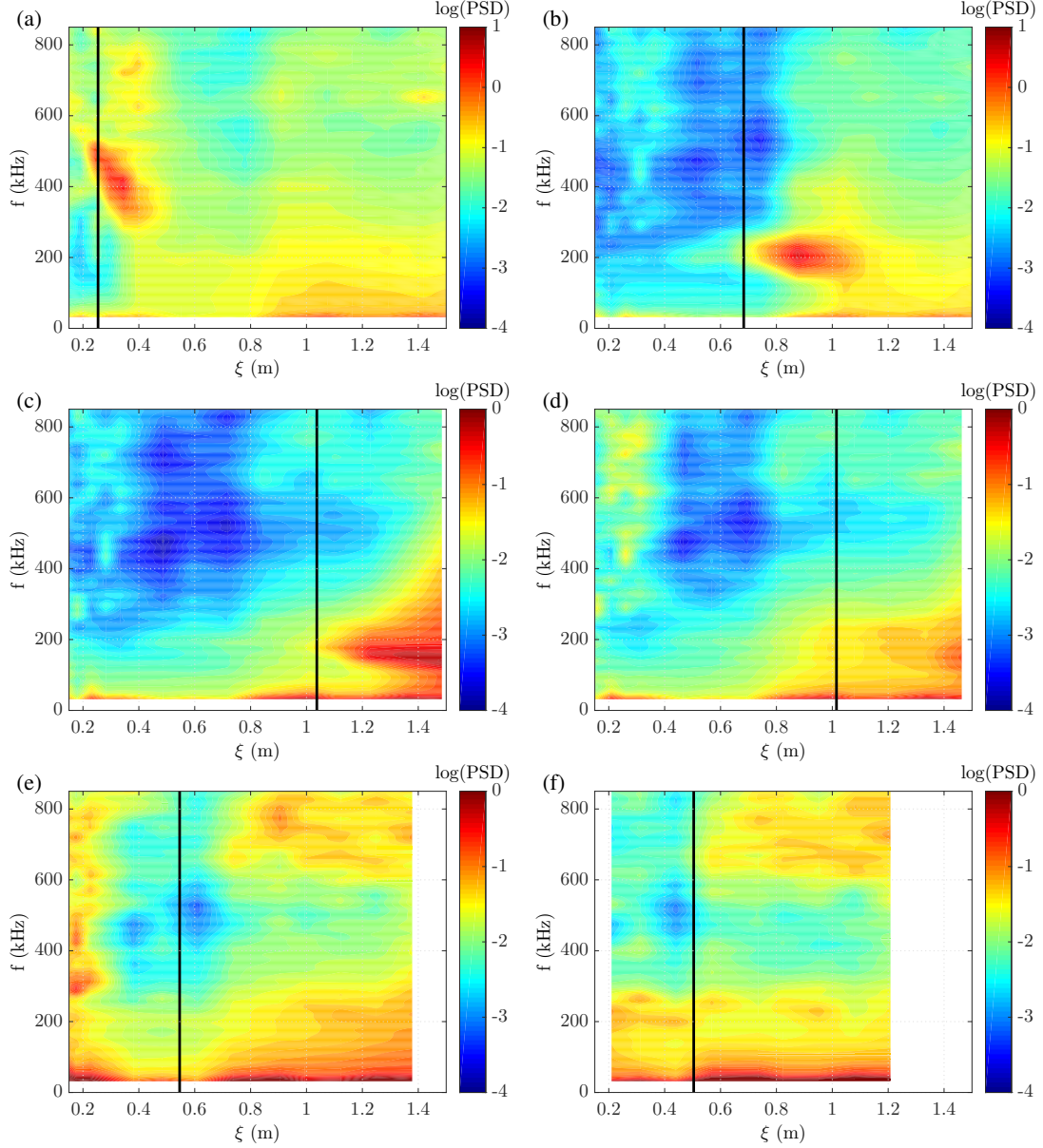
Fig. 4 Contour map of the logarithm of the pressure power spectral density $\log(\text{PSD})$ **for cones with (a)** $R_N = 0.15$ **mm** ($\xi_T = 0.254$ **m), (b)** $R_N = 5.1$ **mm** ($\xi_T = 0.683$ **m), (c)** $R_N = 9.5$ **mm** ($\xi_T = 1.037$ **m), (d)** $R_N = 12.7$ **mm** ($\xi_T = 1.015$ **m), (e)** $R_N = 25.4$ **mm** ($\xi_T = 0.546$ **m), and (f)** $R_N = 50.8$ **mm** ($\xi_T = 0.504$ **m), at** $Re_\infty \approx 17 \times 10^6$ **m^{-1} at Mach** 10 **in Tunnel** 9. **The vertical, black line denotes the measured transition location.**
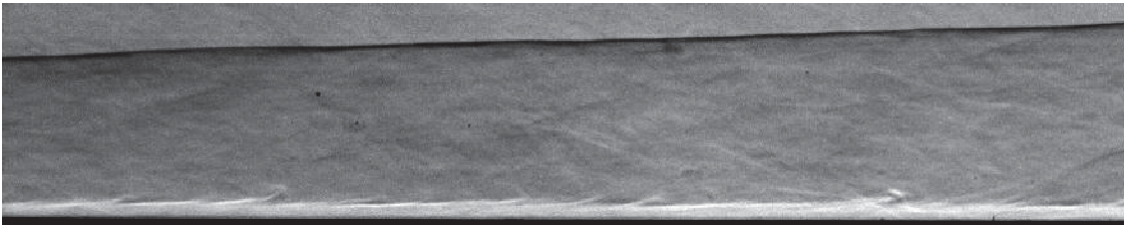
Fig. 5 LIF-based schlieren flow visualization on 4.75 **mm radius nosetip** 7° **half-angle cone in VKI at** $M_\infty = 11.9$ **and** $Re_\infty = 11.6 \times 10^6$ **m^{-1}. Fields of view extend from** $x = 625$ **mm until the end of the cone at** 806 **mm. Disturbance extending past the boundary-layer thickness are visible.**

12

candidate for the experimentally-observed trend in laminar-turbulent transition.

III. Transient Growth Analysis for Hypersonic Blunt Cones

This section presents the transient growth analysis of blunt circular cones with conditions selected to match a subset of the configurations from the experiments conducted by Stetson [2] in the Air Force Research Laboratory (AFRL) Mach 6 High Reynolds Number facility and by Marineau [25] in the Arnold Engineering Development Complex (AEDC) Tunnel 9 at Mach 10. Modal instability analysis for the AFRL configurations has been already performed by Jewell & Kimmel [36], and Marineau [25] has described similar analysis for the AEDC configurations. They found that both first-mode and Mack-mode waves were either damped or weakly unstable for the present configurations; and therefore, transition reversal cannot be predicted with the modal analysis. Another modal instability mechanism that might play a role in the transition reversal is the entropy-layer instability [41, 42]. However, although not shown here, our analysis did not revealed any substantially amplified entropy-layer modes for the configurations of interest. Therefore, the transient growth mechanism is investigated as a potential cause for the transition reversal. First, the basic state solutions are presented in subsection III.A. Second, the transient growth theory is briefly introduced in subsection III.B. Then, a detailed transient growth analysis of the selected blunt cones configurations is presented in subsection III.C.

A. Laminar Boundary Layer over Blunt Cones

The basic states used in the present analysis correspond to the laminar boundary layer flow over the selected blunt cone configurations. The laminar boundary layer flows were computed by Jewell & Kimmel [36] and Marineau [25] with reacting, axisymmetric Navier-Stokes equations on a structured grid. The solver was a version of the NASA data parallel-line relaxation (DPLR) code [43], that is included as part of the STABL-2D software suite, as described by Johnson [44] and Johnson et al. [45]. This flow solver employs a second-order-accurate finite-volume formulation. The inviscid fluxes are based on the modified Steger-Warming flux vector splitting method with a monotonic upstream-cente scheme for the conservation laws (MUSCL) limiter. The time integration method is the implicit, first-order data parallel line relaxation (DPLR) method. Additional details about the basic state solution and the grid convergence study are given by Jewell & Kimmel [36] for the AFRL configurations and by Marineau [25] for the AEDC configurations.

1. AFRL Configurations

The AFRL Mach 6 facility operates at stagnation pressures p_0 from 700 to 2100 psi (4.83 to 14.5 MPa). The working fluid is air and is treated as ideal gas because of the relatively low temperature and pressure. The blunt cones used in the experiments have a half-angle of 8° and a base radius of 2.0 in. (0.0508 m). A total of 196 experiments encompassing 108 unique conditions comprised the Stetson [2] Mach 6 results. Table 1 shows the details of the four configurations selected for the present analysis. The present analysis uses the 7° half-angle variable-bluntness cone

that is currently used in the experiments in the AFRL Mach 6 facility. The thermal wall condition is isothermal with a constant wall temperature equal to $\bar{T}_w$ = 300.0 K.

Table 1   Details of the four AFRL configurations used in the present study. The wall temperature is $\bar{T}_w$ = 300 K. The measured transition locations, ξ_T, are extracted from Ref. [46].

R_N (mm)	Re_∞ ($\times 10^6$ m^{-1})	M_∞	$\bar{T}_\infty$	$\bar{T}_w/\bar{T}_{w,ad}$	ξ_T (m)
5.080	91.4	5.9	76.74	0.57	0.161
15.24	91.4	5.9	76.74	0.57	0.051
15.24	60.9	5.9	76.74	0.57	0.227
15.24	30.5	5.9	76.74	0.57	–

The streamwise evolution of the boundary layer thickness δ_h and edge Mach number M_e is plotted in Fig. 6. The boundary-layer edge, $\eta_e = \delta_h$, is defined as the wall-normal position where $h_t/h_{t,\infty} = 0.995$, with h_t denoting the total enthalpy, i.e., $h_t = h + 0.5(\bar{u}^2 + \bar{v}^2 + \bar{w}^2)$, where h is the static enthalpy. The evolution of boundary layer thickness δ_h within the nose region and along the entire geometry is shown in Figs. 6(a) and 6(b), respectively. The boundary layer thickness is nearly constant from the stagnation point up to $\phi \approx 30°$, which is characteristic of stagnation boundary layer flow. From $\phi \approx 45°$, the boundary layer thickness grows monotonically up to the end of the cone, as shown in Fig. 6(b). Figures 6(a) and 6(b) also show that the boundary layer thickness for the smaller nose radius (R_N = 9.53 mm) cone is smaller than for the larger nose radius (R_N = 15.24 mm) cone with the same freestream conditions ($Re_\infty = 91.4 \times 10^6$ m^{-1}). Figures 6(c) and 6(d) show the evolution of the edge Mach number in the nose region and in the entire cone, respectively. The edge Mach number is determined by inviscid theory to the leading order, and therefore, the evolution within the nose is nearly coincident for the four configurations (Fig. 6(c)). However, the edge Mach number evolution is clearly distinguishable from the smaller to the larger nose radius cases when it is plotted against the streamwise coordinate for the entire geometry (Fig. 6(d)). The sonic location, which coincides with the peak of the streamwise mass-flux within the nose [23, 24], is found at $\phi = 41.4°$. The edge Mach number remains below M_e = 3 along the entire geometry for the large nose radius cones and only becomes slightly larger than M_e = 3 at the end of the cone for the smaller nose radius case.

2. AEDC Configurations

The Air Force AEDC Hypervelocity Wind Tunnel No. 9 (Tunnel 9) is a hypersonic, nitrogen gas, blowdown wind tunnel with interchangeable nozzles that allow for testing at Mach numbers of 7, 8, 10, and 14 over a 0.177×10^6 m^{-1} to 158.8×10^6 m^{-1} unit Reynolds number range. A detailed description of the facility can be found in Ref. [25]. The blunt cones used in the experiments of Marineau et al. [25] had a base diameter of 15 in. (0.381 m) and interchangeable nose tips with radius of 0.152 mm to 50.80 mm. The test matrix for the 24 run test program is provided in Ref. [25]. The working fluid is nitrogen at a relatively low temperature and pressure. Thus, the effects of chemistry and molecular
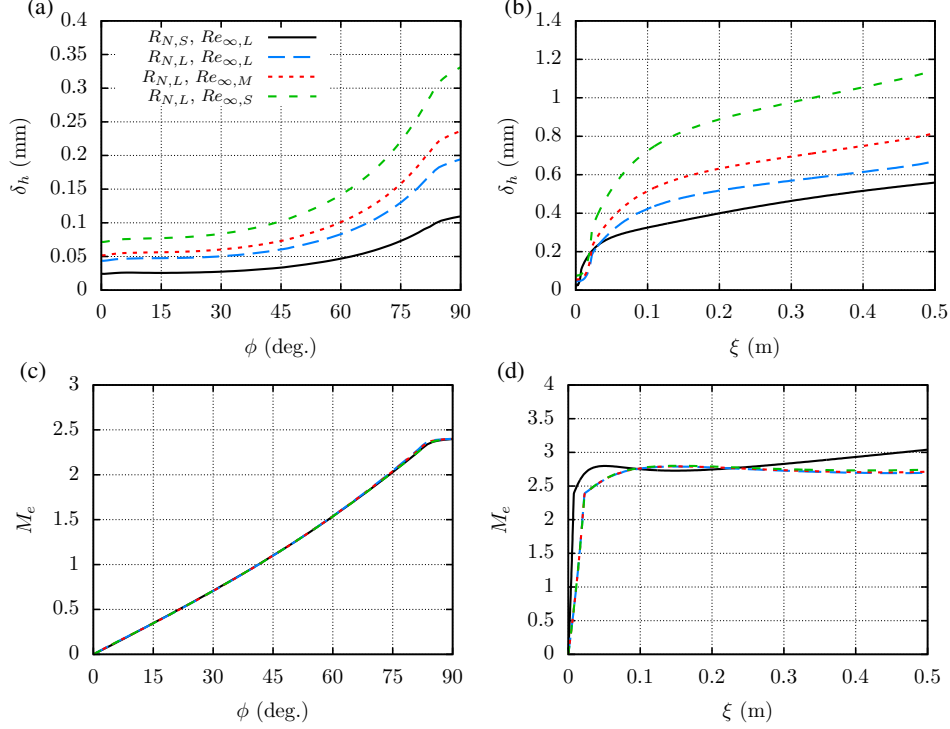
Fig. 6 Streamwise evolution of (a,b) boundary layer thickness and (c,d) edge Mach number of the laminar boundary layer flows over the AFRL configurations. The legend refers to $R_{N,S}$ = 5.08 mm, $R_{N,L}$ = 15.24 mm, $Re_{\infty,L}$ = 91.4 × 10⁶ m⁻¹, $Re_{\infty,M}$ = 60.9 × 10⁶ m⁻¹, $Re_{\infty,S}$ = 30.5 × 10⁶ m⁻¹.

vibration are omitted from the calculations. The viscosity law used is the Sutherland's law and the heat conductivity is calculated using Eucken's relation. Table 2 shows the details of the four configurations selected for the present analysis. The used thermal wall condition is isothermal with a constant wall temperature equal to $\bar{T}_w$ = 300.0 K. The four configurations share a similar freestream unit Reynolds number of $Re_\infty \approx 17.5 \times 10^6$ m⁻¹ and a freestream Mach number of $M_\infty \approx 9.78$. The nose radius values varies from R_N = 9.53 mm to R_N = 50.8 mm.

Table 2   Details of the four AEDC configurations used in the present study. The wall temperature is $\bar{T}_w$ = 300 K. The measured transition locations, ξ_T, are extracted from Ref. [25].

R_N (mm)	Re_∞ (m⁻¹)	M_∞	$\bar{T}_\infty$	$\bar{T}_w/\bar{T}_{w,ad}$	ξ_T (m)
9.530	17.6 × 10⁶	9.797	51.01	0.340	1.037
12.70	17.4 × 10⁶	9.795	51.17	0.339	1.015
25.40	17.3 × 10⁶	9.791	51.13	0.340	0.546
50.80	17.6 × 10⁶	9.777	51.27	0.340	0.504

The boundary layer thickness δ_h and edge Mach number M_e for the four configurations are plotted in Figs. 7(a) and 7(b), respectively. As observed in the comparison of the AFRL configurations of Fig. 6(b), despite the same freestream conditions, the boundary layer thickness in the frustum part of the cone is larger for larger nose radius values. Also, the edge Mach number is larger for the smaller nose radius cases, although remains smaller than M_e = 4.5 for the four
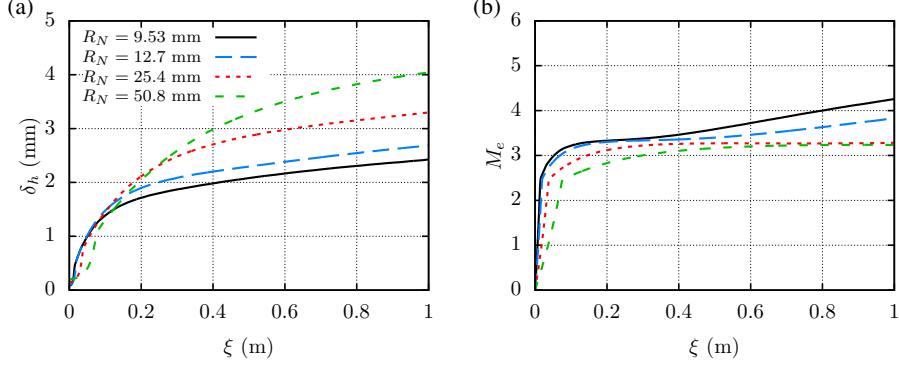
Fig. 7 **Streamwise evolution of (a) boundary layer thickness and (b) edge Mach number of the laminar boundary layer flows over the AEDC configurations.**

configurations.

B. Transient Growth Theory

Transient growth analysis is performed using the linear PSE as explained in the literature [18, 23, 47–49]. The analysis focuses on stationary perturbations because, despite of the speed regime, they experience the largest transient growth. For completeness, the present section outlines the methodology, which bears strong similarities with the optimization approach based on the linearized boundary layer equations [17, 22, 50]. The advantage of the PSE-based formulation is that it is also applicable to more complex base flows where the flow evolves along the streamwise direction and the boundary layer approximation may not hold. The PSE approach can also be easily extended to unsteady disturbances. While infinite Reynolds number asymptotic results cannot be directly computed using this technique, good agreement is achieved between the two methodologies for incompressible and compressible regimes as shown by Paredes et al. [18].

In the PSE context, stationary perturbations have the form

$$\tilde{\mathbf{q}}(\xi, \eta, \zeta) = \hat{\mathbf{q}}(\xi, \eta) \exp\left[i\left(\int_{\xi_0}^{\xi} \alpha(\xi')\,d\xi' + m\zeta - \omega t\right)\right] + \text{c.c.,} \tag{1}$$

where c.c. denotes complex conjugate. The suitably nondimensionalized, orthogonal, curvilinear coordinate system (ξ, η, ζ) denotes streamwise, wall-normal, and azimuthal coordinates and (u, v, w) represent the corresponding velocity components. Density and temperature are denoted by ρ and T. The streamwise and azimuthal wavenumbers are α and m, respectively; and ω is the angular frequency of the perturbation. The Cartesian coordinates are represented by (x, y, z). The vector of perturbation fluid variables is $\tilde{\mathbf{q}}(\xi, \eta, \zeta, t) = (\tilde{\rho}, \tilde{u}, \tilde{v}, \tilde{w}, \tilde{T})^T$ and the vector of amplitude functions is $\hat{\mathbf{q}}(\xi, \eta) = (\hat{\rho}, \hat{u}, \hat{v}, \hat{w}, \hat{T})^T$. The vector of basic state variables is $\bar{\mathbf{q}}(\xi, \eta) = (\bar{\rho}, \bar{u}, \bar{v}, \bar{w}, \bar{T})^T$.

Upon introduction of the perturbation form (1) into the linearized NS equations together with the assumption of a slow streamwise dependence of the basic state and the amplitude functions, thus neglecting the viscous derivatives in ξ,

the PSE are recovered as follows

$$\mathbf{L}\hat{\mathbf{q}}(\xi, \eta) = \left(\mathbf{A} + \mathbf{B}\frac{\partial}{\partial \eta} + \mathbf{C}\frac{\partial^2}{\partial \eta^2} + \mathbf{D}\frac{1}{h_1}\frac{\partial}{\partial \xi}\right)\hat{\mathbf{q}}(\xi, \eta) = 0. \tag{2}$$

The linear operators $\mathbf{A}$, $\mathbf{B}$, $\mathbf{C}$ and $\mathbf{D}$ are given by Pralits et al. [47] and h_1 is the metric factor associated with the streamwise curvature. The system of Eqs. (2) is not fully parabolic due to the term $\partial \hat{p}/\partial \xi$ in the streamwise momentum equation [51–54]. However, for purely stationary disturbances ($\omega = 0$ and $\alpha = 0$), this term can be dropped from the equations as justified in Refs. [48, 55]. For nonstationary perturbations ($\omega \neq 0$), a commonly adopted solution is to replace $\partial \hat{p}/\partial \xi$ by $\Omega_{PNS}\partial \hat{p}/\partial \xi$, where Ω_{PNS} is the Vigneron parameter [56–58]. This parameter was originally introduced for the integration of the parabolized Navier-Stokes equations (PNS) , and is determined by

$$\Omega_{PNS} = \min(1, M_\xi^2), \tag{3}$$

where M_ξ is the local streamwise Mach number. The Vigneron approximation ensures numerical stability of the marching scheme by suppressing upstream influence within the solution. For locally supersonic flow, the equations are not altered because $\Omega_{PNS} = 1$. For a disturbance field with $\alpha \neq 0$, a portion of the elliptic behavior is absorbed in the wave part via the term $i\alpha\hat{p}$ and the residual upstream influence can be suppressed by choosing a sufficiently large marching step [53], without having to invoke the Vigneron approximation.

The optimal initial disturbance, $\tilde{\mathbf{q}}_0$, is defined as the initial (i.e., inflow) condition at ξ_0 that maximizes the objective function, J, which is defined as a measure of disturbance growth over a specified interval $[\xi_0, \xi_1]$. The definitions used in the present study correspond to the outlet energy gain $J = G^{out}$ and mean energy gain $J = G^{mean}$ and are defined as

$$G^{out} = \frac{E(\xi_1)}{E(\xi_0)}, \tag{4}$$

$$G^{mean}\frac{1}{\xi_1 - \xi_0}\frac{\int_{\xi_0}^{\xi_1} E(\xi')\, d\xi'}{E(\xi_0)}, \tag{5}$$

where E denotes the energy norm of $\tilde{\mathbf{q}}$. The energy norm is defined as

$$E(\xi) = \int_\eta \hat{\mathbf{q}}(\xi, \eta)^H \mathbf{M}_E \hat{\mathbf{q}}(\xi, \eta)\, h_1\, h_3\, d\eta, \tag{6}$$

where h_3 is the metric factor associated with the azimuthal curvature, $\mathbf{M}_E$ is the energy weight matrix and the superscript H denotes conjugate transpose. The selection of $J = G^{out}$ corresponds to the "outlet energy gain" that is commonly used in studies of the optimal-perturbation problem [22, 50]. The selection of $J = G^{mean}$ defines the "mean energy gain" and corresponds to the optimization of the mean energy. This latter definition accounts for a possible overshoot

in the disturbance energy evolution that are not accounted for by the former definition and is found to be present in hypersonic blunt forebodies [23, 24], as well as in the nosetip of blunt cones as documented in what follows.

The choice of the energy norm is known to influence the optimal initial perturbation as well as the magnitude of energy amplification [17, 49, 59]. Here, we use the positive-definite energy norm derived by Mack [60] and used by Hanifi et al. [61] for transient growth calculations, which is defined by

$$\mathbf{M}_E = \text{diag} \left[\frac{\bar{T}(\xi, \eta)}{\gamma \bar{\rho}(\xi, \eta) M^2}, \bar{\rho}(\xi, \eta), \bar{\rho}(\xi, \eta), \bar{\rho}(\xi, \eta), \frac{\bar{\rho}(\xi, \eta)}{\gamma(\gamma - 1)\bar{T}(\xi, \eta)M^2} \right]. \tag{7}$$

Additionally, the kinetic energy norm is also used for optimization in this paper. The kinetic energy of a perturbation is defined by

$$K(\xi) = \int_\eta \hat{\mathbf{q}}(\xi, \eta)^H \mathbf{M}_K \hat{\mathbf{q}}(\xi, \eta) \, h_1 \, h_3 \, d\eta, \tag{8}$$

where

$$\mathbf{M}_K = \text{diag} \left[0, \bar{\rho}(\xi, \eta), \bar{\rho}(\xi, \eta), \bar{\rho}(\xi, \eta), 0 \right]. \tag{9}$$

To differentiate when the total energy norm E or the kinetic energy norm K are used, a corresponding subscript is added to the energy gain, resulting in four options for the objective function: G_E^{out}, G_E^{mean}, G_K^{out}, and G_K^{mean}. In the present study, the transient growth amplification is also expressed in terms of the logarithmic amplification ratio, the so-called N-factor, based on the total energy norm, which is defined as

$$N_E = \frac{1}{2} \ln \left(G_E^{out} \right) = - \int_{\xi_0}^\xi \alpha_i(\xi') \, d\xi' + 1/2 \ln \left[\hat{E}(\xi)/\hat{E}(\xi_0) \right]. \tag{10}$$

Furthermore, the present study uses the N-factor based in other disturbance magnitude norms, as the kinetic energy, N_K, maximum temperature, N_T, or maximum streamwise velocity, N_u. These definitions are equivalent to that of Eq. (10), but with their respective norms.

The variational formulation of the problem to determine the maximum of the objective functional J leads to an optimality system [18], which is solved in an iterative manner, starting from a random solution at ξ_0 that must satisfy the boundary conditions. The PSE, $\mathbf{L}\tilde{\mathbf{q}} = 0$, are used to integrate $\tilde{\mathbf{q}}$ up to ξ_1, where the final optimality condition is used to obtain the initial condition for the backward adjoint PSE integration, $\mathbf{L}^\dagger \tilde{\mathbf{q}}^\dagger = c_{mean} F(\tilde{\mathbf{q}})$, where $c_{mean} = 0$ for the outlet energy gain optimization and $c_{mean} = 1$ for the mean energy gain optimization, and $F(\tilde{\mathbf{q}})$ is a function of the direct solution [47]. At ξ_0, the adjoint solution is used to calculate the new initial condition for the forward PSE integration with the initial optimality condition. The iterative procedure finishes when the value of G has converged up to a certain tolerance, which was set to 10^{-4} in the present computations.

Nonuniform stable high-order finite-difference schemes [62, 63] of sixth order are used for discretization of the

PSE along the wall-normal coordinate. The discretized PSE are integrated along the streamwise coordinate by using second-order backward differentiation. The number of discretization points in both directions was varied in selected cases to ensure convergence of the optimal gain predictions. The wall-normal direction was discretized using $N_y = 161$, with the nodes being clustered toward the wall [63]. No-slip, isothermal boundary conditions are used at the wall, i.e., $\hat{u} = \hat{v} = \hat{w} = \hat{T} = 0$. The amplitude functions are forced to decay at the farfield boundary by imposing the Dirichlet conditions $\hat{\rho} = \hat{u} = \hat{w} = \hat{T} = 0$, unless otherwise stated. The farfield boundary coordinate is set just below the shock layer. Verification of the present optimal growth module against available transient growth results from the literature is shown in Ref. [18].

In what follows, we study the axisymmetric boundary layer over circular cones in hypersonic freestream flows. The freestream conditions and geometries are selected to match a subset of configurations used in the experiments conducted at AFRL [2, 36] and at AEDC [25]. For this problem, the computational coordinates, (ξ, η, ζ), are defined as an orthogonal body-fitted coordinate system. The metric factors are defined as

$$h_1 = 1 + \kappa\eta, \tag{11}$$

$$h_3 = r_b + \eta\cos(\theta), \tag{12}$$

where κ denotes the streamwise curvature, r_b is the local radius, and θ is the local half-angle along the axisymmetric surface, i.e., $\sin(\theta) = dr_b/d\xi$. For our study, the half angle, θ, is 7° and $\kappa = 0$ in the frustum region. The end of the nose and beginning of the frustum is denoted as the juncture location that is defined as $\xi_j = R_N\pi/2$. The streamwise coordinate within the nosetip region is represented by an angular coordinate defined as $\phi = \xi/R_N$. The nosetip Reynolds number, $Re_{R_N} = \bar{\rho}_\infty\bar{u}_\infty R_N/\mu_\infty$ is used to scale the energy gain. The length scale $L_{R_N} = R_N/\sqrt{Re_{R_N}}$ is used to normalize the spanwise disturbance wavelength defined as $\lambda = 2\pi r_b/m$.

C. Transient Growth Results

For a nonselfsimilar boundary layer such as the boundary layer over blunt cones, both the initial and final locations must be varied in order to obtain the overall picture of the optimal growth characteristics [23]. A special feature of the transient growth analysis for the blunt cones of interest is that the results naturally split into two parts, one that deals with transient growth intervals that are limited to the nose region, where the results are expected to resemble those for the hemisphere forebody reported by Paredes et al. [23], and a second one that deals with transient growth intervals that extend into the frustum region, where transition is observed in the experiments. Detailed transient growth results are first presented for the AFRL configurations in subsections III.C.1 and III.C.2. Because stationary disturbances usually yield the highest transient growth overall, a majority of the analysis in section III is focused on the zero frequency case. However, motivated by the findings of Cook et al. [64], who performed a resolvent analysis of a similar blunt cone
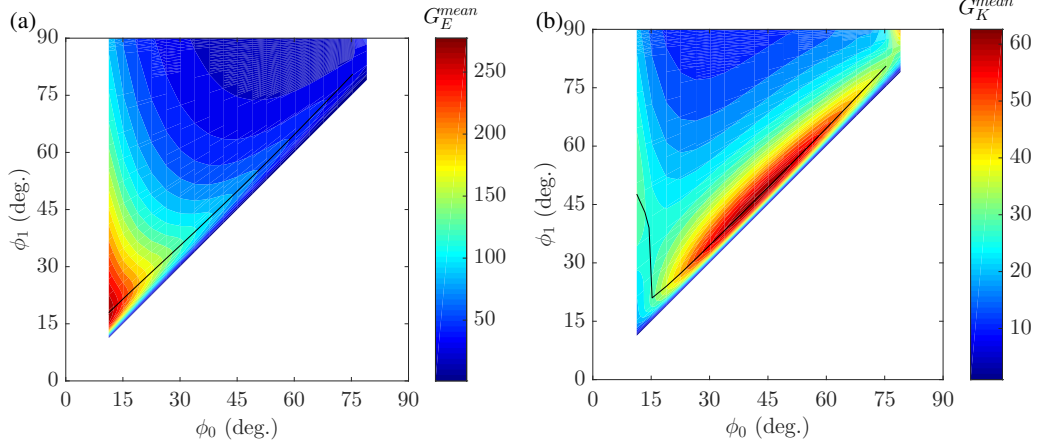
Fig. 8 **Contours of (a) optimal mean total energy gain G_E^{mean} and (b) optimal mean kinetic energy gain G_K^{mean} within the nose region of the $R_N = 15.24$ mm and $Re_\infty = 91.4 \times 10^6$ m^{-1} case. The solid line in the contour plot indicates the value of ϕ_1 corresponding to maximum energy gain for a given ϕ_0.**

configuration at hypersonic conditions and reported significant nonmodal growth of planar, traveling waves inside the entropy layer, the transient growth analysis is extended to traveling disturbances in subsection III.C.3. Finally, a brief summary of results is presented for the AEDC configurations in subsection III.C.4.

1. Transient Growth Interval within the Nose Region

Herein, transient growth results with initial and final disturbance locations within the nose region for the AFRL configurations introduced in Table 1 are investigated. The optimal mean total energy gain (G_E^{mean}) and optimal mean kinetic energy gain (G_K^{mean}) for the $R_N = 15.24$ mm and $Re_\infty = 91.4 \times 10^6$ m^{-1} case are plotted in Figs. 8(a) and 8(b), respectively. Figure 8(a) shows that the highest total energy gain occurs for relatively short optimization intervals in the vicinity of the stagnation point, as indicated by the black line nearly parallel to the lower boundary of the plot. However, the kinetic energy budget for these perturbations initiated near the stagnation point is rather small. This fact is confirmed by the optimal mean kinetic energy gain (G_K^{mean}) plot of Fig. 8(b). The optimal kinetic energy gain exhibits a maximum in the interior of the domain at $\phi_0 = 42.4°$ that nearly coincides with the sonic location, $\phi_{Me=1} = 41.4°$. These results indicate the same features as the results reported by Paredes et al. [23] for a hypersonic hemisphere forebody.

The optimal growth results for a specified inflow location ξ_0 of the flow are characterized in terms of the combination of azimuthal wavenumber m and outflow location ξ_1 that lead to the maximum value of the energy gain. Thus, the effect of nosetip radius R_N on the maximum value of the optimal energy gain, optimal wavenumber, and optimal growth interval, is analyzed next. Figure 9 shows the optimal total and kinetic energy gains as a function of the inflow location (Figs. 9(a) and 9(d)), as well as the corresponding azimuthal wavenumber (Figs. 9(b) and 9(e)) and the optimal growth interval (Figs. 9(c) and 9(f)). Results are shown for the $R_N = 5.08$ mm and $R_N = 15.24$ mm cones at the same freestream unit Reynolds number of $Re_\infty = 91.4 \times 10^6$ m^{-1}. Figure 9(a) shows that both the total and kinetic energy
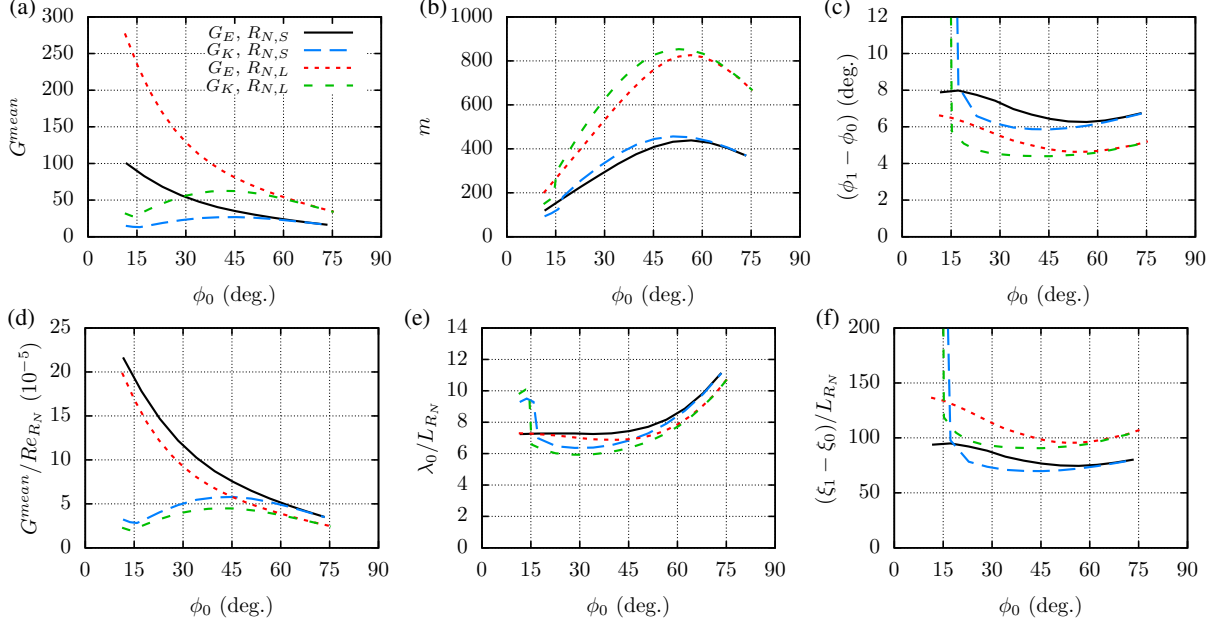
Fig. 9 **(a,d) Optimal mean energy gain and corresponding (b,e) azimuthal wavenumber and (c,f) optimization interval within the nose region for $R_{N,S}$ = 5.08 mm and $R_{N,L}$ = 15.24 mm cones at same freestream unit Reynolds number, $Re_\infty = 91.4 \times 10^6$ m^{-1}.**

gains are larger for the larger nose radius, although as shown in Fig. 9(d), the scaling is not perfectly linear because, as indicated by Paredes et al. [24], small deviations from the linear scaling occur as a result of the differences in the ratio of boundary-layer thickness to the radius of the surface curvature. Figure 9(b) shows that the optimal azimuthal wavenumber is nearly twice as large for the larger nose radius cone in comparison with the case of the smaller nose radius. The scaling of the initial disturbance wavelength with L_{R_N} plotted in Fig. 9(e) shows a reasonable scaling with the boundary layer thickness. On the other side, the optimal growth interval plotted in Fig. 9(c) does not scale with L_{R_N} (or R_N) as shown in Fig. 9(f), presumably because the ratio of boundary-layer thickness to the radius of the surface curvature plays an important role for this parameter.

2. Transient Growth along the Frustum Region

Next, transient growth across spatial intervals that extend into the frustum region is studied in detail for the AFRL configurations. In this case, we find it more convenient to plot the transient growth amplification in terms of the N-factor based on the total energy norm defined in Eq. (10). Figures 10(a) shows the N-factor contours for initial and final locations on the frustum for the R_N = 5.08 mm AFRL cone at $Re_\infty = 91.4 \times 10^6$ m^{-1}. Similar results for the larger nose radius, R_N = 15.24 mm, are shown in Fig. 10(b). The N-factor values are larger for the smaller nose radius cone except for initial and final locations near the juncture of the cone, i.e., beginning of the frustum. The N_E values are larger than 5.5 in the studied range of parameters for the smaller nose radius case (Fig. 10(a)). For the larger nose radius case, the N_E values are larger than 4.5 in the range of ξ_0 and ξ_1 values studied here, although the N_E = 3.5 value is
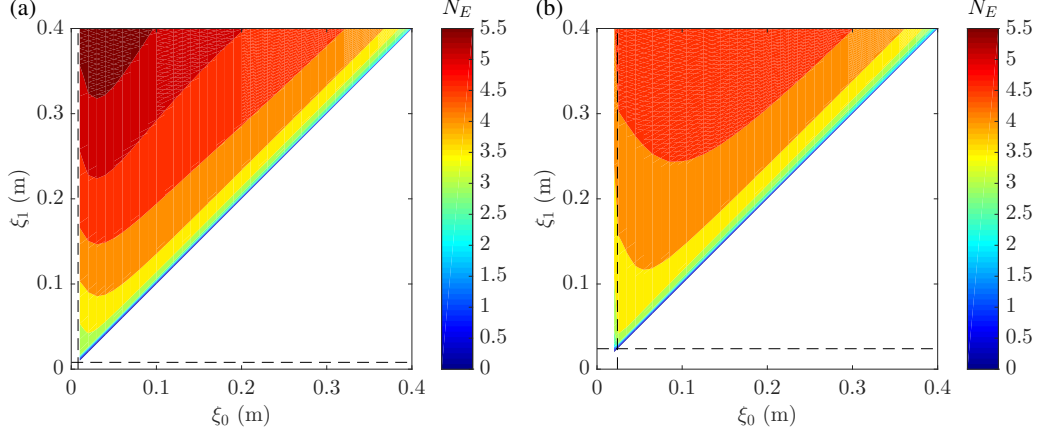
21

Fig. 10 **Contours of N-factor values defined as $N_E = 1/2\ln(G_E^{out})$ in the frustum region of the (a) $R_N = 5.08$ mm and (b) $R_N = 15.24$ mm cones. The juncture location ξ_j is marked with a vertical and a horizontal dashed line. The freestream unit Reynolds number is $Re_\infty = 91.4 \times 10^6$ m^{-1}.**

reached at smaller values of ξ_1 than for the smaller radius case when the initial disturbance location is near the juncture location $\xi_0 \approx \xi_j$.

Figures 11(a) and 11(b) show a magnified view of the N-factor contours from Figs. 10(a) and 10(b), respectively, for initial and final locations in the vicinity of the juncture between the nose and the frustum of the cone. Both figures show different behavior of the transient growth amplification for disturbances initiated within the nose region ($\xi_0 < \xi_j$) and those that are initiated downstream of the juncture location ($\xi_0 \geq \xi_j$). The disturbances initiated in the nose have a maximum for very short optimal growth intervals, as previously shown in Fig. 9. For larger optimal growth intervals, the transient growth amplification first decreases and then increases again for $\xi_1 > \xi_j$. On the other side, disturbances initiated downstream of the nose ($\xi_0 \geq \xi_j$) experience a monotonic increase in energy gain factor as ξ_1 is increased. Remarkably, disturbances initiated in the vicinity of the juncture location ($\xi_0 \approx \xi_j$) experience a quite rapid growth for the blunter case and short transient growth intervals (Fig. 11(b)), resulting in relatively significant values of N_E just downstream of the juncture location.

The AFRL experiments investigated the effect of an azimuthally-periodic array of roughness elements mounted near the sonic point at $\phi = 45°$. To help gain some insight into the role of transient growth as a mechanism for roughness effects, we next examine the details of transient growth disturbances initiated in the nose region at $\phi_0 = \xi_0/R_N = 45°$, which coincides with the location of the roughness array. A description of the experimental findings is deferred to section IV. Figure 12 shows the mean total energy gain and corresponding azimuthal wavenumber as a function of the optimal growth interval, $\Delta\xi = \xi_1 - \xi_0$, for the four AFRL configurations shown in Table 1. Figure 12(a) shows that the trend previously observed for $\xi_0 < \xi_j$ at $Re_\infty = 91.4 \times 10^6$ m^{-1} (Fig. 11(b)) also applies at other Reynolds numbers. Specifically, the optimal energy gain has a maximum immediately downstream of the inflow station and then decays up to a plateau zone before increasing again for longer transient growth intervals. For the same freestream unit
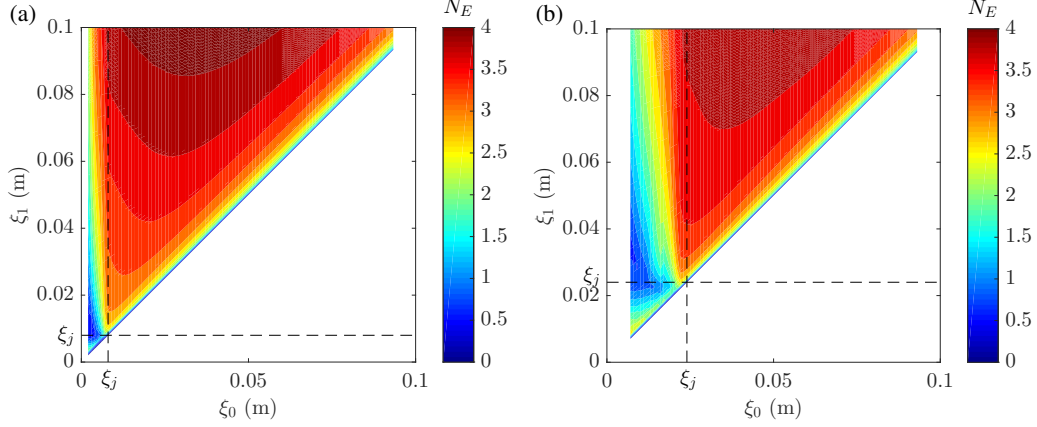
Fig. 11 **Contours of N-factor values defined as $N_E = 1/2\ln(G_E^{out})$ in the vicinity of the nose region of the (a) $R_N = 5.08$ mm and (b) $R_N = 15.24$ mm cones. The juncture location ξ_j is marked with a vertical and a horizontal dashed line. The freestream unit Reynolds number is $Re_\infty = 91.4 \times 10^6$ m^{-1}.**

Reynolds number, the initial peak in optimal energy gain is larger for the larger nose radius cone than for the smaller nose radius case, but this situation is reversed for larger optimal growth intervals ($\Delta\xi > 0.02$ m). Figure 12(b) shows that the three regions translate into a discontinuous evolution of the corresponding azimuthal wavenumber. The scaling of the optimal mean total energy gain with Re_{R_N} (Fig. 12(c)) and of the corresponding initial azimuthal wavelength with L_{R_N} (Fig. 12(d)) is reasonable for the cases with same nose radius $R_N = 15.24$ mm and different freestream unit Reynolds numbers, but not for the smaller nose radius case ($R_N = 5.08$ mm) and outside the nose region.

Figure 13 shows further details of the transient growth disturbances initiated in the nose at $\phi_0 = 45°$ for the blunter cone at the highest Re_∞ configuration ($R_N = 15.24$ mm and $Re_\infty = 91.4 \times 10^6$ m^{-1}). Three cases based on the trends observed in Fig. 12 are plotted; namely, (A) $\Delta\xi = 0.0030$ m and $m = 420$; (B) $\Delta\xi = 0.023$ m and $m = 150$; and (C) $\Delta\xi = 0.091$ m and $m = 80$. The case (A) corresponds to the first peak in mean energy gain that is larger for the larger nose radius cone (Fig. 12(a)). The evolution of the disturbance amplitude $\sqrt{E/E_0}$ for the case (A) shows a rapid rise to its peak value within a rather short distance from the initial disturbance location and a slower subsequent decay with values lower than 1 for streamwise locations in the frustum region. The initial optimal perturbation plotted in Fig. 13 is mostly contained within the boundary layer thickness; and hence, such initial disturbance profiles are better suited for excitation via surface roughness than some other cases where the initial profiles extend well outside of the boundary layer. The disturbance amplitude evolution of the case (B) has a smaller initial peak and then remains below 6 along the streamwise domain plotted in Fig. 13. The initial optimal perturbation associated with this case (B) is similar to that in case (A), but the peaks of the perturbation variables are located somewhat farther from the wall, which presumably makes this perturbation less likely to be excited via surface roughness. The energy gain evolution for case (C) ($\Delta\xi = 0.091$ m, $m = 80$) shows rather small disturbance amplification near the inflow location and then a monotonic amplification up to $\xi = 0.2$ m. Figure 13 shows that the optimal initial perturbation shape in case (C) is more complex
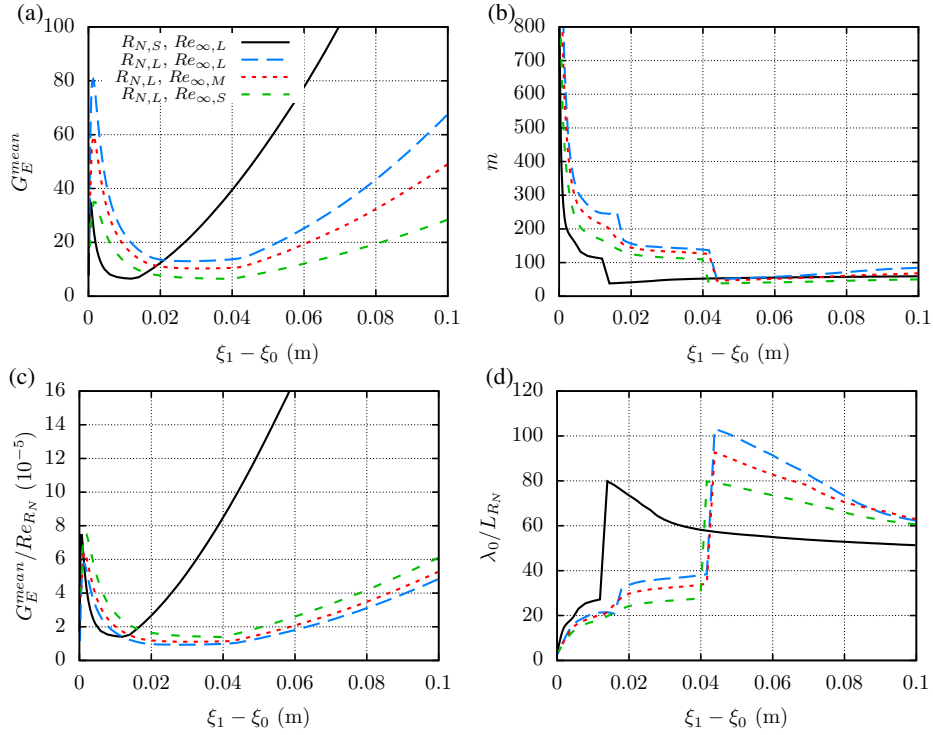
Fig. 12 (a,c) **Optimal mean energy gain and corresponding** (b,d) **azimuthal wavenumber with initial distur-bance location** $\phi_0 = 45°$ ($\xi_0 = 0.04$ **m for the** $R_N = 5.08$ **mm cone and** $\xi_0 = 0.012$ **m for the** $R_N = 15.24$ **mm cone). The legend refers to** $R_{N,S} = 5.08$ **mm,** $R_{N,L} = 15.24$ **mm,** $Re_{\infty,L} = 91.4 \times 10^6$ **m**$^{-1}$**,** $Re_{\infty,M} = 60.9 \times 10^6$ **m**$^{-1}$**,** $Re_{\infty,S} = 30.5 \times 10^6$ **m**$^{-1}$**.**
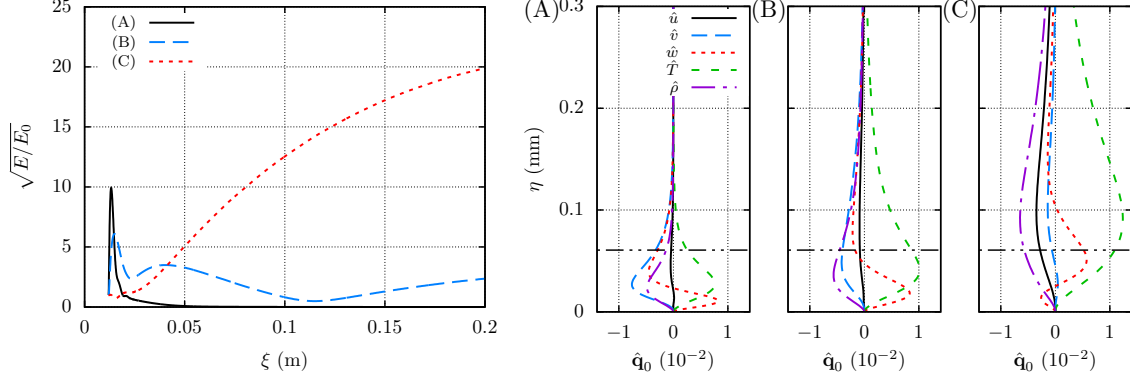
Fig. 13   Evolution of the disturbance amplitude $\sqrt{E/E_0}$ and corresponding initial optimal perturbations for the R_N = 15.24 mm and $Re_\infty = 91.4 \times 10^6$ m^{-1} configuration. The selected optimization intervals and azimuthal wavenumbers are (A) $\Delta\xi$ = 0.0030 m and m = 420; (B) $\Delta\xi$ = 0.023 m and m = 150; and (C) $\Delta\xi$ = 0.091 m and m = 80. The initial disturbance location is set at the nosetip at $\phi_0 = 45°$ that corresponds to $\xi_0 = 0.012$ m. The horizontal, dash-double dot lines indicates the edge of the boundary layer based on total enthalpy, $\eta = \delta_h$.

than that for cases (A) and (B), because the perturbation profiles for wall-normal and spanwise velocity components have two and three peaks instead of one and two peaks, respectively. Also, the perturbation profiles have a larger wall-normal extension and the peaks of these profiles are located farther from the wall. In summary, the results shown in Fig. 13 indicate that roughness-induced perturbations at $\phi_0 = 45°$ can experience transient growth in a short interval within the nose region. The transient growth streaks can lead to the onset of nonstationary streak instabilities that typically amplify rather rapidly and induce transition shortly after their onset; see Refs. [65–70] for details on secondary instability of streaks in high-speed boundary layers.

Previously, disturbances initiated in the vicinity of the juncture location, $\xi_j = R_N\pi/2$, were found to experience a larger growth for the larger nose radius cone and relatively short transient growth intervals. This finding is further investigated here. Figure 14 shows the mean gain in total energy and corresponding azimuthal wavenumber as a function of the optimal growth interval, $\Delta\xi = \xi_1 - \xi_0$, for the four AFRL configurations shown in Table 1. Figure 14(a) shows in details that the trend observed in Fig. 11(b) is for $Re_\infty = 91.4 \times 10^6$ m^{-1} is also found at other Reynolds numbers. Specifically, the energy gain has a monotonic increasing evolution as $\Delta\xi$ is increased, and the energy gain is larger for larger nose radius for relatively short optimization intervals ($\Delta\xi < 0.13$ m). The difference between the energy gain values for the two nose radii (R_N = 5.08 and 15.24 mm) and same freestream unit Reynolds number ($Re_\infty = 91.4 \times 10^6$ m^{-1}) reaches about a factor of 2 for $\Delta\xi = 0.05$ m. The azimuthal wavenumbers associated with the optimal energy gain values of Fig. 14(a) are shown in Fig. 14(b). The azimuthal wavenumber quickly decreases and as the length of the transient growth interval increases, albeit at a decreasing rate. Compared to the large bluntness cases (R_N = 15.24 mm), the smaller radius case (R_N = 5.08 mm, $Re_\infty = 91.4 \times 10^6$ m^{-1}) shows a notable, different behavior of both the optimal energy gain and the associated azimuthal wavenumbers. This difference is clearly observed in the scaled mean energy gain and scaled initial wavelength plotted in Figs. 14(c) and 14(d), respectively. The large nose radius cases
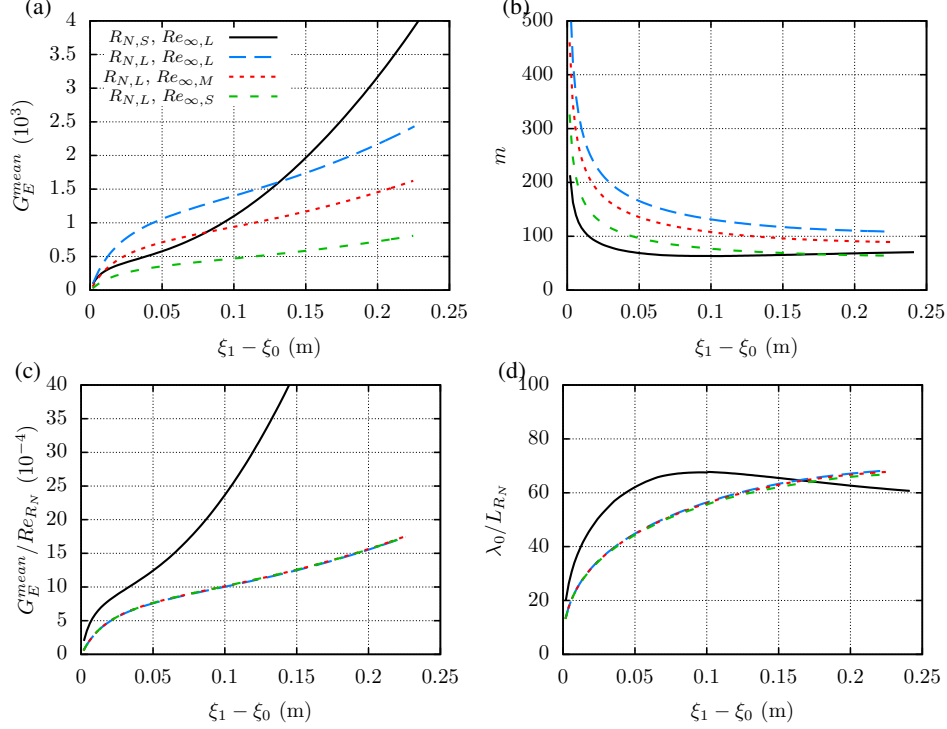
**Fig. 14 (a,c) Optimal mean energy gain and corresponding (b,d) azimuthal wavenumber with initial distur-
bance location set in the juncture at $\xi_0 = \xi_j = R_N\pi/2$ ($\xi_0 = 0.008$ m for $R_N = 5.08$ mm and $\xi_0 = 0.024$ m
for $R_N = 15.24$ mm.) The legend refers to $R_{N,S} = 5.08$ mm, $R_{N,L} = 15.24$ mm, $Re_{\infty,L} = 91.4 \times 10^6$ m^{-1},
$Re_{\infty,M} = 60.9 \times 10^6$ m^{-1}, $Re_{\infty,S} = 30.5 \times 10^6$ m^{-1}.**

($R_N = 15.24$ mm) show a perfect scaling of both properties as the unit Reynolds number is varied, but the scaled values

corresponding to the small radius case ($R_N = 5.08$ mm) are clearly different from the blunt nose cases. The reason for

this poor scaling of the transient growth parameters with nose radius could be due to the lack of selfsimilarity of the

boundary layer profiles near the nose.

Figure 15 shows further details of the transient growth disturbances initiated at the juncture location for the

$R_N = 15.24$ mm and $Re_\infty = 91.4 \times 10^6$ m^{-1} configuration. The three cases shown in Fig. 15 for the $R_N = 15.24$ mm

case correspond to (A) $\Delta\xi = 0.0295$ m and $m = 200$; (B) $\Delta\xi = 0.0668$ m and $m = 150$; and (C) $\Delta\xi = 0.2066$ m and

$m = 110$. Figure 15 shows that the peak in disturbance amplitude moves slightly downstream as the optimal growth

interval becomes longer from case (A) to case (C). This peak is barely reached at the end of the cone length for the

case (C). The optimal initial perturbations associated with the three cases are plotted in Fig. 15. The wall-normal

extension and the peaks of these profiles are located closer to the wall for shorter optimal growth intervals, which makes

them more closely related to roughness-induced perturbations. A wall-mounted device is not expected to generate a

perturbation with the wall-normal extension of the optimal perturbation corresponding to case (C). Although not shown

here, equivalent results for the small radius case ($R_N = 5.08$ mm, $Re_\infty = 91.4 \times 10^6$ m^{-1}) and an optimal growth interval

of $\Delta\xi = 0.0295$ m show a peak disturbance amplitude equal to approximately one half of the peak value corresponding
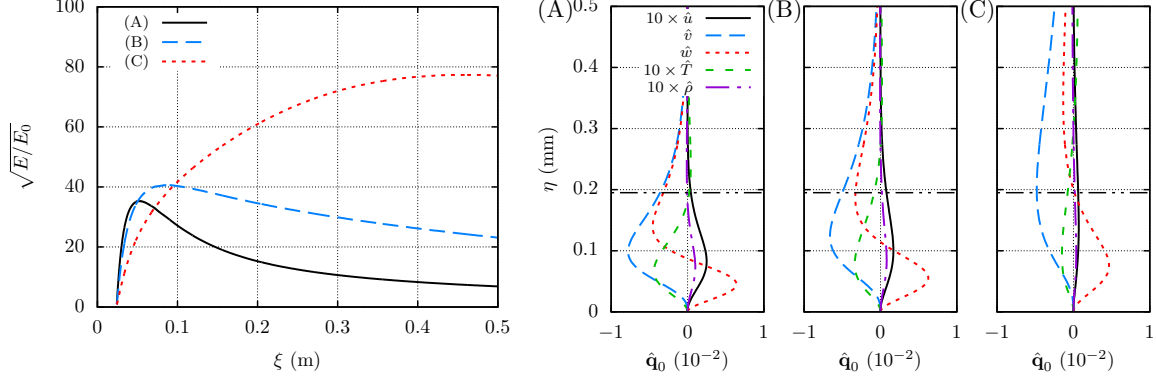
Fig. 15 **Evolution of the disturbance amplitude $\sqrt{E/E_0}$ and corresponding initial optimal perturbations for the $R_N = 15.24$ mm and $Re_\infty = 91.4 \times 10^6$ m^{-1} configuration. The selected optimization intervals and azimuthal wavenumbers are (A) $\Delta\xi = 0.0295$ m and $m = 200$; (B) $\Delta\xi = 0.0668$ m and $m = 150$; and (C) $\Delta\xi = 0.2066$ m and $m = 110$. The initial disturbance location is set at the juncture $\xi_0 = \xi_j$ that corresponds to $\xi_0 = 0.024$ m. The horizontal, dash-double dot lines indicates the edge of the boundary layer based on total enthalpy, $\eta = \delta_h$.**

to the large radius cone ($R_N = 15.24$ mm, $Re_\infty = 91.4 \times 10^6$ m^{-1}) plotted in Fig. 15. Similar to results for disturbances initiated near the sonic location, these results with $\xi_0 = \xi_j$ indicate that roughness-induced perturbations can experience greater transient growth for larger nosetip bluntness at the same freestream conditions. Therefore, transition onset could be driven by roughness-induced transient growth if the streak amplitude required for streak instabilities is reached.

3. Transient Growth of Traveling Disturbances along the Frustum Region

Next, we present salient findings pertaining to the nonmodal growth of traveling disturbances over the frustum region of the AFRL cone for the case of $R_N = 5.08$ mm and $Re_\infty = 91.4 \times 10^6$ m^{-1}. A detailed parameter study of traveling mode disturbances is deferred to Paredes et al. [71]. The procedure used for the transient growth analysis of traveling disturbances is the same as that used earlier for the stationary disturbances with $\alpha = 0$, except with the addition of the streamwise pressure gradient term that is approximated with Eq. (3) based on the work by Vigneron et al. [56] for PNS equations. For the results presented herein, we confine our attention to a transient growth interval of $(\xi_0; \xi_1) = (0.04; 0.161)$ m. The selected outflow location corresponds to the transition location measured by Jewell et al. [46] as indicated in Table 1, whereas the inflow location was chosen on the basis of a parameter study, which showed that the maximum energy gain occurs for $\xi_0 = 0.04$ m for most combinations of frequency and azimuthal wavenumber.

Figure 16 shows the contours of the N-factor based on the total energy gain, N_E, as a function of the frequency, F, and azimuthal wavenumber, m. The outlet energy gain is selected as the objective function for the optimal growth analysis. One may observe that the maximum energy gain of $N_E = 4.59$ is achieved by a stationary, three-dimensional perturbation with $F = 0.0$ kHz and $m = 82$. This stationary disturbance is the same as that studied previously in section III.C.2. Additionally, Fig. 16 shows a second, local maximum ($N_E = 3.27$) in the N-factor contours for planar traveling waves with $F = 340.0$ kHz, $m = 0$. Additional results not presented herein for sharper cones ($R_N = 1.524$ and
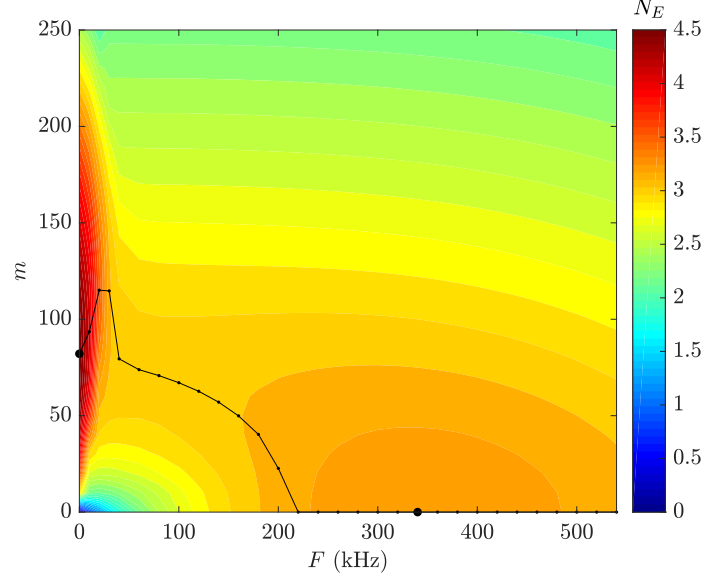
Fig. 16 Contours of N-factor values defined as $N_E = 1/2\ln(G_E^{out})$ in the azimuthal wavenumber versus frequency plane in the frustum region of the $R_N = 5.08$ mm cone with $Re_\infty = 91.4 \times 10^6$ m^{-1}, $\xi_0 = 0.04$ m and $\xi_1 = \xi_T = 0.161$ m. The isocontours represents N-factor increments of $\Delta N_E = 0.1$. The solid black line denotes the azimuthal wavenumber corresponding to maximum N_E. The large black circles denote the (F, m) combination for maximum N_E in both axes.

2.54 mm) have indicated that the energy gain associated with this local maximum for traveling disturbances increases with the nose bluntness. Those results also showed that, unlike the case considered in Fig. 16, the peak N-factor for traveling disturbances is not always associated with planar waves.

Figures 17 and 18 show further details concerning the streamwise evolution of the optimal traveling disturbance ($F = 340.0$ kHz, $m = 0$, $(\xi_0; \xi_1) = (0.04; 0.161)$ m and $J = G_E^{out}$). Figure 17 illustrates the axial growth in the disturbance amplitude in terms of the N-factors based on the total energy (N_E), kinetic energy (N_K), maximum temperature fluctuation (N_T), and the maximum of the streamwise velocity fluctuation N_u, respectively. To check the grid convergence of the solution obtained on the basis of $\alpha = 0$ and the PNS approximation, results were obtained with two different streamwise grids with $n_\xi = 8192$ and $n_\xi = 16384$, respectively. To confirm that the Vigneron parameter does not have a significant influence on the N-factor evolution, additional results were obtained by marching the PSE equations with the same initial condition. The PSE solution is obtained without invoking the Vigneron PNS approximation (i.e., with $\alpha \neq 0$ and $\Omega_{PNS} = 1$). The number of streamwise points required to obtain grid converged results with $\alpha \neq 0$ is approximately two orders of magnitude lower than the number of grid points required to resolve the entire wave form via $\alpha = 0$. The agreement between the various results is excellent, indicating that the prediction accuracy is not compromised by either physical or numerical approximation. An important characteristic of the traveling mode growth is the large difference between the growth factors for the temperature and streamwise velocity perturbations, respectively. The maximum N-factor based on the temperature perturbation is $N_T = 6.82$, whereas that based on the
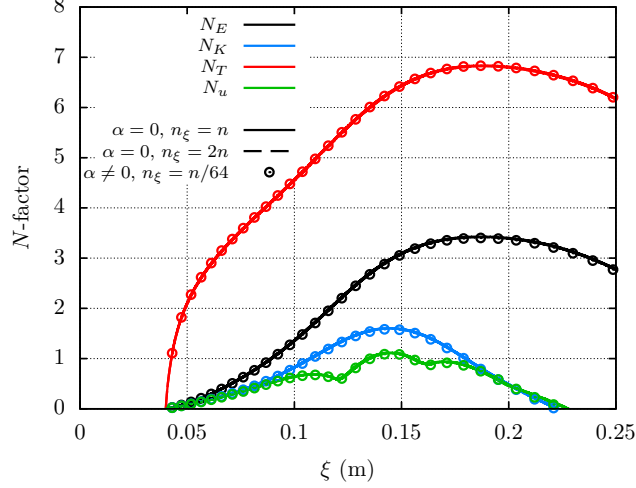
Fig. 17 *N*-factor evolution of the optimal disturbance with $F = 340$ **kHz,** $m = 0$, $\xi_0 = 0.04$ **m, and** $\xi_1 = 0.161$ **m, for the** $R_N = 5.08$ **mm cone with** $Re_\infty = 91.4 \times 10^6$ **m^{-1}. The solid and dashed lines represent the solution with** $\alpha = 0$ **and PNS approximation of Eq.** (3) **with** $n_\xi = n = 8192$ **points and** $n_\xi = 2n$**, respectively. The symbols denotes the solution with** $\alpha \neq 0$ **and no PNS approximation (**$\Omega_{PNS} = 1$**).**

streamwise velocity perturbation is substantially lower, $N_u = 1.11$. This difference is also reflected in the evolution of the total disturbance energy and the disturbance kinetic energy, indicating that the transient growth of the traveling disturbances is mainly reflected in the thermodynamic perturbations. The optimum initial disturbance at the inflow location is dominated by velocity fluctuations, which are an order of magnitude larger than the temperature fluctuations. However, the rapid growth in temperature perturbation immediately downstream of the inflow location allows the velocity and temperature perturbation to become comparable to each other. Indeed, Paredes et al. [71] have pointed out that, because of the sustained higher growth in temperature perturbation over the remaining portion of the transient growth interval (albeit at a reduced pace in comparison with the inflow region), the temperature fluctuations become the dominant component of the outflow disturbance at $\xi = \xi_1$. On the basis of initial value analysis of transient nonmodal growth in compressible Poiseuille flows, Xie et al. [72] argued that the pressure-velocity coupling at higher Mach numbers played an important role in influencing the evolution of disturbances that are nearly aligned with the mean flow direction. However, the role of temperature fluctuations was not directly investigated. Therefore, further work will be necessary to establish whether or not the physical mechanisms discussed therein also play a role in the transient growth of planar disturbances observed in this paper.

The streamwise evolution in the mode shape of the optimal disturbance is plotted in Figure 18. The normalized temperature $\tilde{T}/\max(\tilde{T})$ and streamwise velocity $\tilde{u}/\max(\tilde{u})$ are mostly contained between the boundary-layer edge δ_h and the entropy-layer edge, δ_S, which is defined as the location where the local entropy increment with respect to the freestream value, i.e., $\Delta S = c_p \ln(\bar{T}/\bar{T}_\infty) - R_g \ln(\bar{p}/\bar{p}_\infty)$, is 0.25 times the entropy increment at the wall ($\Delta S(\xi, \eta = \delta_S) = 0.25 \Delta S_{wall}$). The disturbance is initially tilted against the flow direction and increases in magnitude
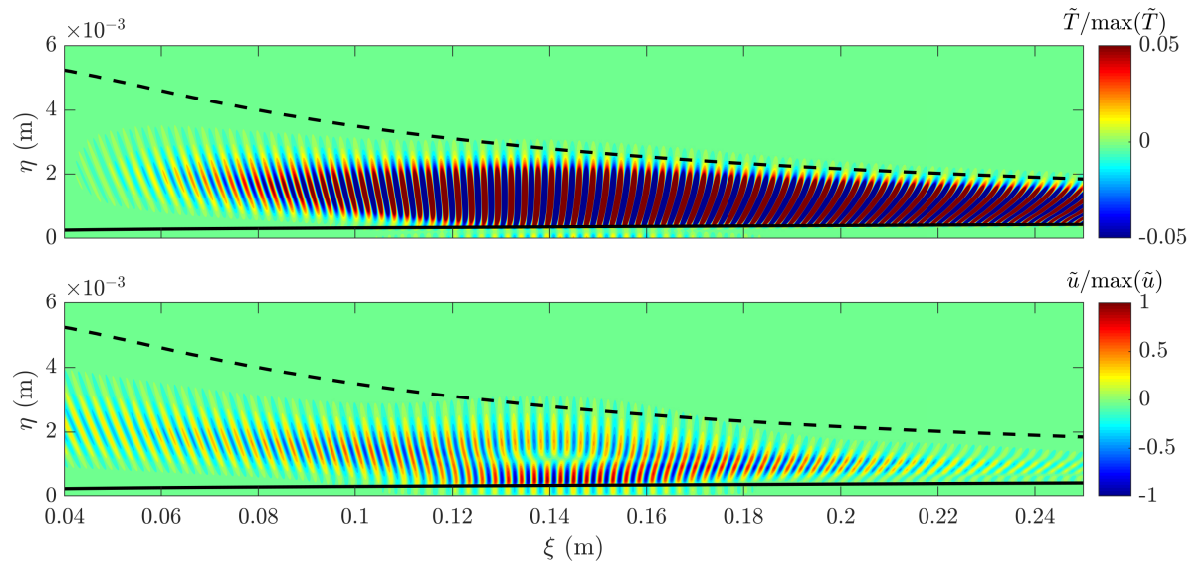
Fig. 18 Contours of normalized temperature and streamwise velocity components of the optimal disturbance with F = 340 kHz, $m = 0$, ξ_0 = 0.04 m, and ξ_1 = 0.161 m, for the R_N = 5.08 mm cone with Re_∞ = 91.4 × 10⁶ m⁻¹. The solid, black line indicates the edge of the boundary layer, δ_h. The dashed, black line indicates the edge of the entropy layer, δ_S.

while rotating downstream. This behavior strongly resembles to the Orr mechanism for the transient growth of planar disturbances [73, 74], which has been widely studied for incompressible flows [20, 75]. Nonmodal growth based on the Orr mechanism is attributed an energy extraction from the mean shear by transporting momentum down the mean momentum gradient through the action of the Reynolds stress associated with the perturbation field. However, the energy amplification observed in this compressible case is mainly attributed to the temperature perturbation within the entropy layer. Similar to the LIF-based schlieren images of Fig. 5, the peak disturbance magnitude at any axial location is observed outside of the mean boundary layer edge. However, additional work is required to establish a more definitive link between the experimental observations and the nonmodal growth mechanism reported herein. Furthermore, because the traveling mode structure in Fig. 18 has a relatively weak signature within the boundary layer region, its role in initiating boundary layer transition also remains to be clarified. Similarly, nonlinear simulations of these traveling instabilities, e.g., by means of nonlinear PSE, could provide some insights into the potential breakdown mechanism and the minimum initial amplitude of the optimal disturbance that would likely result in the onset of transition at the measured transition location.

4. Transient Growth on AEDC Configurations

Transient growth results for the AFRL cones showed that disturbances initiated in the vicinity of the juncture between the nosetip and the frustum of the cone can experience a rather strong transient amplification in a short streamwise distance. This amplification is stronger for the larger nose radius case at same freestream conditions. Based on that
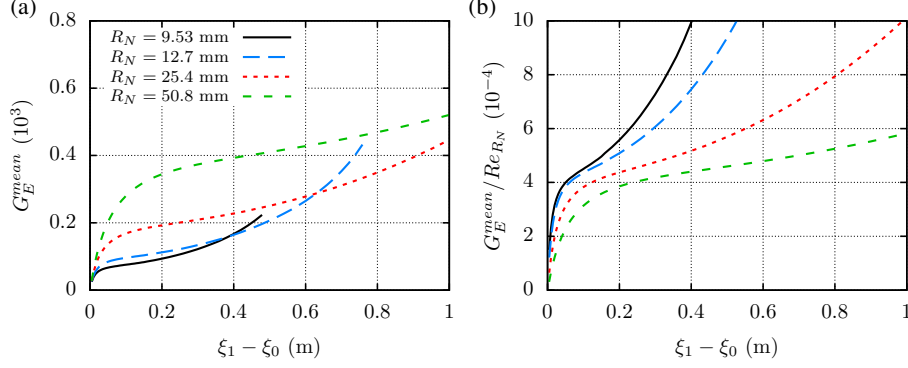
Fig. 19 Optimal mean energy gain with initial disturbance location set at the juncture $\xi_0 = \xi_j = R_N \pi/2$ for the AEDC configurations ($\xi_0 = 0.015$ m for $R_N = 9.53$ mm, $\xi_0 = 0.020$ m for $R_N = 12.7$ mm, $\xi_0 = 0.040$ m for $R_N = 25.4$ mm, and $\xi_0 = 0.080$ m for $R_N = 50.8$ mm). The freestream unit Reynolds number is $Re_\infty \approx 17.5 \times 10^6$ m^{-1}.

observation, results for the AEDC configurations are focused on disturbances initiated at the juncture of the cones to study the trend with this different set of flow and geometry parameters. Figure 19(a) shows the evolution of optimal gain in mean energy gain as a function of the optimal growth interval for disturbances initiated at the juncture location. Again, as the nose radius of the cone is increased, the optimal energy gain becomes notably larger. Figure 19(b) indicates that the scaled energy gain values, G_E^{mean}/Re_{R_N}, are smaller for larger nose radius cases, indicating a nonlinear increase in optimal energy gain with increasing nose bluntness. This trend is similar to the trend in Fig. 14(c) for the AFRL configurations.

IV. Roughness Effects on Laminar-Turbulent Transition on Blunt Cones

Between 1978 and 1982, K. F. Stetson performed a total of 196 sharp- and blunt-cone experiments on a thin-walled 8° half-angle, 4 in. (0.1016 m) diameter base cone at zero angle of attack in the AFRL Mach 6 High Reynolds Number facility. These measurements were initially reported in a 1983 paper [2] and recently Jewell & Kimmel [36] performed a computational analysis indicating that neither the Mack second mode nor the first mode were likely to be the dominant instability mechanism for nosetips with radius larger than 1 mm, for which transition was nevertheless consistently observed once sufficient freestream Reynolds numbers were reached. Alternate physical mechanisms may explain these results, and include transient growth or mean flow distortion from roughness.

More recently, experiments have been performed in the same facility on a 7° half-angle variable-bluntness cone at zero angle of attack with similar nosetip bluntness values, which have also been shown to transition from laminar to turbulent flow without significant predicted amplification of first- or second-mode instability for smooth nosetips with radius larger than 1 mm and sufficient freestream Reynolds numbers [46]. A subset of the smooth cases, with $R_N = 5.08$ mm and $R_N = 15.24$ mm, have been repeated with 15 μm laser-machined roughness elements of approximately cubical shape located on the circle at 45 degrees from the apex of the spherical tip, which is near the sonic line for zero angle of

attack. The array of roughness elements has been designed following the transient growth results of subsection III.C. The number of roughness elements has been selected to match the disturbance azimuthal wavenumber that lead to significant transient growth at the same conditions. Specifically, 210 roughness elements were mounted on the small radius cone (R_N = 5.08 mm) and 420 roughness elements on the large radius cone (R_N = 15.24 mm). A picture of the small radius nosetip with the array of roughness elements is shown in Fig. 20.

Fig. 20   Nosetip of R_N = 5.08 mm with 210 equally spaced 15 μm cubical roughness elements that were laser-machined circumferentially at $45°$ from the apex of the spherical tip.

The presence of roughness elements on the R_N = 5.08 mm cone had little discernible effect on the experimentally observed transition location or heating levels across the operating conditions of the Mach 6 Hi Re Facility. In contrast, roughness elements of the same shape and dimension on the R_N = 15.24 mm cone had a profound effect on transition above a critical Reynolds number. This effect is illustrated in Figs. 21(a) and 21(b), which present surface heat flux distributions measured by Medtherm coaxial thermocouples from pairs of rough and smooth experiments, with roughness-height Re_{kk} values matched to within 3% between the two sets. In Fig. 21(a), the rough (Re_∞ = 66.5 × 10^6 m^{-1}, k/δ_h = 0.381, Re_{kk} = 294) and smooth (Re_∞ = 66.0 × 10^6 m^{-1}) surface heat transfer values for the R_N = 5.08 mm cone overlap. In Fig. 21(b), the rough (Re_∞ = 75.8 × 10^6 m^{-1}, k/δ_h = 0.225, Re_{kk} = 287) and smooth (Re_∞ = 76.9 × 10^6 m^{-1}) cases for the R_N = 15.24 mm cone are quite different, with the rough tip resulting in nearly immediate transition onset, while the equivalent smooth tip results in laminar flow nearly to the end of the cone. This result indicates that the onset of transition in this data is associated with the combined effects of bluntness and roughness.

V. Summary and Concluding Remarks

A collaborative effort by the NATO STO group AVT-240 on Hypersonic Boundary-Layer Transition Prediction was devoted to bluntness effects on transition over circular cones at zero angle of attack. This paper presented an overview of that work, which consisted of transition measurements on blunt cones models with varying degrees of nosetip bluntness, measurements pertaining to the combined effects of nose bluntness and controlled surface roughness on the nose tip, and theoretical analysis of optimal transient growth on blunt cones.

The following observations can be made on the basis of wind tunnel measurements at freestream Mach numbers
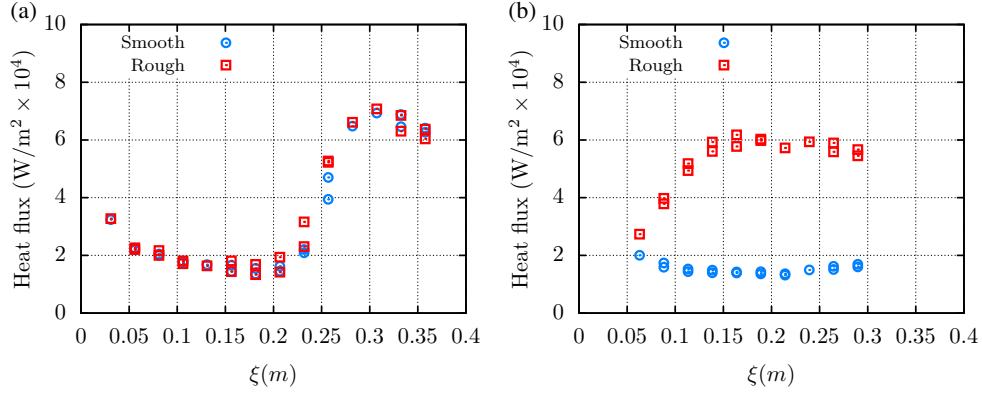
Fig. 21 **Heat flux distributions for a** $7°$ **half-angle cone at** $M_\infty = 5.9$ **with nosetip of (a)** $R_N = 5.08$ **mm and (b)** $R_N = 15.24$ **mm for a smooth tip and a tip with a row of equally spaced** 15 μm **cubical roughness elements.**

from 6 to 12:

1) The recent measurements are consistent with the known trend of an initially downstream movement in the transition onset location as the nosetip bluntness is increased. This trend confirms the stabilizing effect of nose bluntness on the amplification of Mack mode, i.e., second-mode instability waves.

2) The measurements also confirm the well-known observation concerning a reversal in the above trend at sufficiently large value of the nosetip Reynolds number and the transition reversal phenomenon cannot be explained via the hydrodynamic stability paradigm, due to the absence of an adequately significant modal amplification of first-mode, second-mode, and entropy-layer instabilities.

3) Experimental measurements indicate that, in the transition reversal regime, boundary layer transition over the frustum of the cone is highly sensitive to wall roughness. The onset of transition appears to be dominated by disturbances that originate in the vicinity of the nosetip, suggesting roughness-induced transient growth as a likely cause for laminar-turbulent transition.

Optimal transient growth analysis has been conducted for the laminar flow based on the solution of the Navier-Stokes equations over a $7°$ half-angle variable-bluntness cone at zero angle of attack with bluntness and freestream conditions corresponding to a subset of the experiments of Stetson [2] at the AFRL Mach 6 High Reynolds Number facility and $Re_\infty = 30.5 - 91.4 \times 10^6$ m^{-1} and of Marineau et al. [25] at the AEDC Tunnel 9 facility with the Mach 10 nozzle and $Re_\infty \approx 17.5 \times 10^6$ m^{-1}. Some interesting findings in regard to the transient growth of both stationary and traveling disturbances have been uncovered in the course of this study. Estimates of maximum possible transient growth are obtained through a dual optimization [23, 24] that varies both the initial and final locations of the transient growth interval. The following conclusions may be drawn on the basis of the transient growth analysis:

1) The optimal growth results can be naturally divided into two parts. The first part deals with transient growth intervals limited to the nose region, and second part applies to optimal growth intervals that extend to the frustum region that encompasses the range of measured transition locations.

2) Results for optimal growth intervals within the nose region are similar to the findings by Paredes et al. [23] for a hemispherical forebody. Specifically, the highest predicted growth in total energy corresponds to relatively short transient growth intervals in the vicinity of the stagnation point, but the kinetic energy growth associated with these perturbations is rather small. The maximum growth in disturbance kinetic energy is found for perturbations initiated near the sonic point at an angle of 42.4° from the apex of the spherical tip. Furthermore, the wall-normal profiles of optimal initial perturbations associated with the maximum energy gain are concentrated within the boundary layer thickness, i.e., close to the wall. More important, at a fixed set of freestream conditions, increased nose bluntness results in higher transient amplification within the nose region.

3) Based on the transient growth analysis for both AFRL and AEDC configurations, one may conclude that stationary disturbances that are initiated in the vicinity of the juncture between the nosetip and the frustum also exhibit a greater transient amplification for larger values of nosetip bluntness, but only for relatively short optimization intervals. Furthermore, for the large nosetip bluntness, the wall-normal extension of the optimal initial perturbations is small, indicating that wall roughness may be able to induce such perturbations.

4) The transient growth analysis of traveling disturbances showed significant growth of planar waves that peak between the boundary-layer and entropy edges. The temperature component of the disturbance can reach significant N-factors at the measured transition location, $N_T \approx 7$, while the streamwise velocity component is barely amplified, $N_u \approx 1$.

We note that the actual generation (i.e., receptivity) of the transient growth disturbances has not been addressed in this paper. Disturbance profiles resulting from realistic external disturbances usually result in a suboptimal transient growth. In that regard, the present results based on optimal initial, disturbances may be viewed as providing an upper bound on the nonmodal amplification due to either spanwise periodic, roughness-induced, stationary disturbances or freestream traveling waves.

Finally, the roughness effects on transition reversal over a 7° half-angle blunt cone at hypersonic flow are experimentally investigated in the AFRL Mach 6 High Reynolds Number facility. Transition measurements were made with an azimuthally periodic array of 15 μm, laser-machined roughness elements of approximately cubical shape located at 45° from the apex of the spherical tip, which nearly coincides with the sonic location. The roughness array spacing ($m = 210$ for $R_N = 5.08$ mm and $m = 420$ for $R_N = 15.24$ mm) was designed to match the disturbance azimuthal wavenumber that is predicted to induce large transient growth under the respective conditions. The following observations can be made on the basis of these measurements:

1) The roughness array on the small nosetip bluntness cone showed no effect on the transition location at $Re_\infty \approx 66 \times 10^6$ m^{-1} (i.e., $k/\delta_h = 0.381$, $Re_{kk} = 294$).

2) On the other hand, the experiments conducted with the large nosetip bluntness with $Re_\infty \approx 76 \times 10^6$ m^{-1} (i.e., $k/\delta_h = 0.225$, $Re_{kk} = 287$) showed a prominent effect of the roughness elements on the transition onset, moving

the transition front close to the nosetip, whereas the smooth tip baseline for the same blunter cone has resulted in a laminar flow over the majority of the cone.

3) The above findings indicate that the transition onset is associated with the combined effects of bluntness and roughness.

Finally, we note that wakes behind sufficiently large discrete roughness elements can sustain large modal amplification of streak instabilities as shown by Choudhari et al. [65, 67]; but the level of amplification is sensitive to the roughness parameters and other flow details [66]. Because the measured onset of transition during the AFRL experiments was within a short distance behind the roughness array, wake instability may have played a role in the large upstream shift in transition location; and we are currently investigating that possibility via more detailed computations. However, a broader set of measurements involving controlled surface roughness would be useful in determining whether or not naturally occurring micro-roughness over the model surface may have been responsible for the observed transition reversal in other blunt cone experiments. Effects of roughness location in the vicinity of the nosetip and the juncture location would be an important aspect of such a parametric study. Flow visualizations accompanied by dynamic measurements, i.e., high frequency response heat transfer or pressure measurements, in the region between the controlled surface roughness and the onset of transition would go a long way in providing valuable clues regarding the physical mechanisms at play. Finally, performing parallel measurements in both quiet and conventional wind tunnel facilities, or in flight test experiments, would provide further information regarding the role of both the freestream disturbances and the nonmodal growth of traveling disturbances within the entropy layer during transition reversal phenomenon.

Acknowledgments

References

[1] Schneider, S., "Hypersonic laminar-turbulent transition on circular cones and scramjet forebodies," *Progress in Aerospace Sciences*, Vol. 40, 2004, pp. 1–50. doi:10.1016/j.paerosci.2003.11.001.

[2] Stetson, K., "Nosetip bluntness effects on cone frustum boundary layer transition in hypersonic flow," AIAA Paper 83-1763, 1983. doi:10.2514/6.1983-1763.

[3] Morkovin, M., Reshotko, E., and Herbert, T., "Transition in open flow systems - A reassessment," *Bull. Am. Phys. Soc.*, Vol. 39, 1994, p. 1882.

[4] Reshotko, E., "Boundary layer transition, instability and control," AIAA Paper 94-0001, 1994. doi:10.2514/6.1994-0001.

[5] Reshotko, E., and Tumin, A., "Spatial theory of optimal disturbances in a circular pipe flow," *Phys. Fluids*, Vol. 13, 2001, pp. 991–996. doi:10.1063/1.1352624.

[6] Avila, K., Moxey, D., De Lozar, A., Avila, M., Barkely, D., and Hof, B., "The onset of turbulence in pipe flow," *Science*, Vol. 333, 2011, pp. 192–196. doi:10.1126/science.1203223.

[7] Reshotko, E., "Preliminary experimental study of disturbances in a laminar boundary layer due to distributed surface roughness," AIAA Paper 81-1224, 1981. doi:10.2514/6.1981-1224.

[8] White, E., "Transient growth of stationary disturbances in a flat plate boundary layer," *Physics of Fluids*, Vol. 14, No. 12, 2002, pp. 4429–4439. doi:10.1063/1.1521124.

[9] Sharp, N., and White, E., "Roughness-induced transient growth on a hypersonic blunt cone," AIAA Paper 2014-0432, 2014. doi:10.2514/6.2014-0432.

[10] Murphy, J., and Rubesin, M., "Re-evaluation of heat-transfer data obtained in flight test of heat-sink shielded re-entry vehicles," *Journal of Spacecraft Rockets*, Vol. 3, No. 1, 1966, pp. 53–60. doi:10.2514/3.28385.

[11] Reshotko, E., and Tumin, A., "The blunt body paradox: A case for transient growth," *Laminar-Turbulent Transition: IUTAM Symposium, Sedona/AZ September 13 – 17, 1999*, edited by H. Fasel and W. Saric, Springer Berlin Heidelberg, Berlin, Heidelberg, 2000, pp. 403–408. doi:10.1007/978-3-662-03997-7_60.

[12] Schneider, S., "Hypersonic boundary-layer transition on blunt bodies with roughness," AIAA Paper 2008-0501, 2008. doi:10.2514/6.2008-501.

[13] Hollis, B., "Blunt-body entry vehicle aerothermodynamics: transition and turbulent heating," *Journal of Spacecraft Rockets*, Vol. 49, No. 3, 2012, pp. 435–449. doi:10.2514/1.51864.

[14] Case, K., "Stability of inviscid plane Couette flow," *Physics of Fluids*, Vol. 3, 1960, pp. 143–148. doi:10.1063/1.1706010.

[15] Stuart, J., "The production on intense shear layers by vortex stretching and convection," NATO AGARD Report No. 514. (also: National Phys. Lab. Aeronaut. Res. Rep. 1147), 1965.

[16] Landahl, M., "A note on algebraic instability of inviscid parallel shear flows," *Journal of Fluid Mechanics*, Vol. 98, 1980, pp. 243–251. doi:10.1017/S0022112080000122.

[17] Tumin, A., and Reshotko, E., "Optimal disturbances in compressible boundary layers," *AIAA Journal*, Vol. 41, 2003, pp. 2357–2363. doi:10.2514/2.6860.

[18] Paredes, P., Choudhari, M., Li, F., and Chang, C.-L., "Optimal growth in hypersonic boundary layers," *AIAA Journal*, Vol. 54, No. 10, 2016, pp. 3050–3061. doi:10.2514/1.J054912.

[19] Schmid, P., and Henningson, D. S., *Stability and Transition in Shear Flows*, Springer, New York, 2001. doi:10.1007/978-1-4613-0185-1.

[20] Schmid, P., "Nonmodal stability theory," *Annual Review of Fluid Mechanics*, Vol. 39, 2007, pp. 129–162. doi:10.1146/annurev.fluid.38.050304.092139.

[21] Reshotko, E., and Tumin, A., "Role of transient growth in roughness-induced transition," *AIAA Journal*, Vol. 42, 2004, pp. 766–770. doi:10.2514/1.9558.

[22] Andersson, P., Berggren, M., and Henningson, D., "Optimal disturbances and bypass transition in boundary layers," *Physics of Fluids*, Vol. 11, 1999, pp. 134–150. doi:10.1063/1.869908.

[23] Paredes, P., Choudhari, M., and Li, F., "Blunt-body paradox and transient growth on a hypersonic spherical forebody," *Physical Review Fluids*, Vol. 2, 2017, p. 053903. doi:10.1103/PhysRevFluids.2.053903.

[24] Paredes, P., Choudhari, M., and Li, F., "Blunt-body paradox and improved application of transient growth framework," *AIAA Journal*, 2018, (to appear).

[25] Marineau, E., Moraru, C., Lewis, D., Norris, J., Lafferty, J., Wagnild, R., and Smith, J., "Mach 10 boundary-layer transition experiments on sharp and blunted cones," AIAA Paper 2014-3108, 2014. doi:10.2514/6.2014-3108.

[26] Aleksandrova, E., Novikova, A., Utyzhnikov, S., and Fedorov, A., "Experimental study of the laminar turbulent transition on a blunt cone," *Journal of Applied Mechanics and Technical Physics*, Vol. 55, No. 3, 2014, pp. 375–385. doi:10.1134/S0021894414030018.

[27] Softley, E., Graber, B., and Zempel, R., "Experimental observation of transition of the hypersonic boundary layer," *AIAA Journal*, Vol. 7, No. 2, 1969, pp. 254–263. doi:10.2514/3.5083.

[28] Softley, E., "Boundary layer transition on hypersonic blunt, slender cones," AIAA Paper 69-0705, 1969. doi:10.2514/6.1969-705.

[29] Stetson, K., "Hypersonic boundary layer transition experiments," AFWAL-TR-80-3062, 1980.

[30] Muir, J., and Trujillo, A., "Experimental investigation of the effects of nose bluntness, free-stream unit Reynolds number, and angle of attack on cone boundary layer transition at a Mach number of 6," AIAA Paper 72-0216, 1972. doi:10.2514/6.1972-216.

[31] Stetson, K., and Rushton, G., "Shock tunnel investigation of boundary layer transition at M=5.5," *AIAA Journal*, Vol. 5, 1967, pp. 899–906. doi:10.2514/3.4098.

[32] Rotta, N., "Effects of nose bluntness on the boundary layer characteristics of conical bodies at hypersonic speeds," NYU-AA-66-66, 1966.

[33] Malik, M., Spall, R., and Chang, C.-L., "Effect of nose bluntness on boundary layer stability and transition," AIAA Paper 90-0112, 1990. doi:10.2514/6.1990-112.

[34] Herbert, T., and Esfahanian, V., "Stability of hypersonic flow over a blunt body," AGARD CP-514. Paper 28. Theoretical and experimental methods in hypersonic flows., 1994.

[35] Marineau, E., "Prediction methodology for second-mode-dominated boundary-layer transition in hypersonic wind tunnels," *AIAA Journal*, Vol. 55, No. 2, 2017, pp. 484–499. doi:10.2514/1.J055061.

[36] Jewell, J., and Kimmel, R., "Boundary layer stability analysis for Stetson's Mach 6 blunt cone experiments," *Journal of Spacecraft Rockets*, Vol. 54, No. 1, 2017, pp. 258–265. doi:10.2514/1.A33619.

[37] Johnson, H., and Gandler, G., "Hypersonic boundary layer stability analysis using PSE-Chem," AIAA Paper 2005-5023, 2005. doi:10.2514/6.2005-5023.

[38] Balakumar, P., and Chou, A., "Transition prediction in hypersonic boundary layers using receptivity and freestream spectra," *AIAA Journal*, Vol. 56, No. 1, 2018, pp. 193–208. doi:10.2514/1.J056040.

[39] Zanchetta, M., "Kinetic heating and transition studies and hypersonic speeds," Ph.D. thesis, Imperial College of Science, Technology and Medicine, London, 1996. URL https://spiral.imperial.ac.uk/handle/10044/1/37124.

[40] Grossir, G., Pinna, F., Bonucci, G., Regert, T., Rambaut, P., and Chazot, O., "Hypersonic boundary layer transition on a 7 degree half-angle cone at Mach 10," AIAA Paper 2014-2774, 2014. doi:10.2514/6.2014-2779.

[41] Dietz, G., and Hein, S., "Entropy-layer instabilities over a blunted flat plate in supersonic flow," *Physics of Fluids*, Vol. 11, No. 1, 1999, pp. 7–9. doi:10.1063/1.869899.

[42] Fedorov, A., and Tumin, A., "Evolution of disturbances in entropy layer on blunted plate in supersonic flow," *AIAA Journal*, Vol. 42, No. 1, 2004, pp. 89–94. doi:10.2514/1.9033.

[43] Wright, M., Candler, G., and Bose, D., "Data-parallel line relaxation method for the Navier-Stokes equations," *AIAA Journal*, Vol. 36, No. 9, 1998, pp. 1603–1609. doi:10.2514/2.586.

[44] Johnson, H., "Thermochemical interactions in hypersonic boundary layer stability," Ph.D. thesis, University of Minnesota, 2000.

[45] Johnson, H., Seipp, T., and Candler, G., "Numerical study of hypersonic reactig boundary layer transition on cones," *Physics of Fluids*, Vol. 10, No. 10, 1998, pp. 2676–2685. doi:10.1063/1.869781.

[46] Jewell, J., Kennedy, R., Laurence, S., and Kimmel, R., "Transition on a variable bluntness 7-degree cone at high Reynolds number," AIAA Paper 2018-1822, 2018. doi:10.2514/6.2018-1822.

[47] Pralits, J., Airiau, C., Hanifi, A., and Henningson, D., "Sensitivity analysis using adjoint parabolized stability equations for compressible flows," *Flow, Turbulence and Combustion*, Vol. 65, 2000, pp. 321–346. doi:10.1023/A:1011434805046.

[48] Tempelmann, D., Hanifi, A., and Henningson, D., "Spatial optimal growth in three-dimensional boundary layers," *Journal of Fluid Mechanics*, Vol. 646, 2010, pp. 5–37. doi:10.1017/S0022112009993260.

[49] Tempelmann, D., Hanifi, A., and Henningson, D., "Spatial optimal growth in three-dimensional compressible boundary layers," *Journal of Fluid Mechanics*, Vol. 704, 2012, pp. 251–279. doi:10.1017/jfm.2012.235.

[50] Luchini, P., "Reynolds-number-independent instability of the boundary layer over a flat surface: Optimal perturbations," *J. Fluid Mech.*, Vol. 404, 2000, pp. 289–309. doi:10.1017/S0022112099007259.

[51] Li, F., and Malik, M., "Mathematical nature of parabolized stability equations," *R. Kobayashi (Ed.), Laminar-Turbulent Transition, Springer*, 1994, pp. 205–212. doi:10.1007/978-3-642-79765-1_24.

[52] Li, F., and Malik, M., "On the nature of the PSE approximation," *Theoretical and Computational Fluid Dynamics*, Vol. 8, No. 4, 1996, pp. 253–273. doi:10.1007/BF00639695.

[53] Li, F., and Malik, M., "Spectral analysis of parabolized stability equations," *Computers & Fluids*, Vol. 26, No. 3, 1997, pp. 279–297. doi:10.1016/S0045-7930(96)00044-8.

[54] Haj-Hariri, H., "Characteristics analysis of the parabolized stability equations," *Studies Applied Mathematics*, Vol. 92, 1994, pp. 41–53. doi:10.1002/sapm199492141.

[55] Bagheri, S., and Hanifi, A., "The stabilizing effect of streaks on Tollmien-Schlichting and oblique waves: A parametric study," *Physics of Fluids*, Vol. 19, 2007, pp. 078103–1–4. doi:10.1063/1.2746047.

[56] Vigneron, Y., Rakich, J., and Tannehill, J., "Calculation of supersonic viscous flow over delta wings with sharp supersonic leading edges," AIAA Paper 78-1137, 1978. doi:10.2514/6.1978-1137.

[57] Chang, C., Malik, M., Erlebacher, G., and Hussaini, M., "Compressible stability of growing boundary layers using parabolized stability equations," AIAA Paper 1991-1636, 1991. doi:10.2514/6.1991-1636.

[58] Chang, C.-L., "Langley Stability and Transition Analysis Code (LASTRAC) Version 1.2 User Manual," NASA TM-2004-213233, 2004.

[59] Zuccher, S., Tumin, A., and Reshotko, E., "Parabolic approach to optimal perturbations in compressible boundary layers," *Journal of Fluid Mechanics*, Vol. 556, 2006, pp. 189–216. doi:10.1017/S0022112006009451.

[60] Mack, L. M., "Boundary layer stability theory," Tech. Rep. Jet Propulsion Laboratory Report 900-277, California Institute of Technology, Pasadena, CA, 1969.

[61] Hanifi, A., Schmid, P., and Henningson, D., "Transient growth in compressible boundary layer flow," *Physics of Fluids*, Vol. 8, 1996, pp. 826–837. doi:10.1063/1.868864.

[62] Hermanns, M., and Hernández, J., "Stable high-order finite-difference methods based on non-uniform grid point distributions," *International Journal for Numerical Methods in Fluids*, Vol. 56, 2008, pp. 233–255. doi:10.1002/fld.1510.

[63] Paredes, P., Hermanns, M., Le Clainche, S., and Theofilis, V., "Order 10^4 speedup in global linear instability analysis using matrix formation," *Computer Methods in Applied Mechanics and Engineering*, Vol. 253, 2013, pp. 287–304. doi: 10.1016/j.cma.2012.09.014.

[64] Cook, D., Thome, J., Brock, J., Nichols, J., and Candler, G., "Understanding effects of nose-cone bluntness on hypersonic boundary layer transition using input-output analysis," AIAA Paper 2018-0378, 2018. doi:10.2514/6.2018-0378.

[65] Choudhari, M., Li, F., and Edwards, J., "Stability analysis of roughness array wake in a high-speed boundary layer," AIAA Paper 2009-0170, 2009.

[66] Choudhari, M., Li, F., Chang, C., Edwards, J., Kegerise, M., and King, R., "Laminar-turbulent transition behind dicrete roughness elements in a high-speed boundary layer," AIAA Paper 2010-1575, 2013. doi:10.2514/6.2010-1575.

[67] Choudhari, M., Li, F., Chang, C., Norris, A., and Edwards, J., "Wake instabilities behind discrete roughness elements in high speed boundary layers," AIAA Paper 2013-0081, 2013. doi:10.2514/6.2013-81.

[68] Paredes, P., Choudhari, M., and Li, F., "Nonlinear transient growth and boundary layer transition," AIAA Paper 2016-3956, 2016. doi:10.2514/6.2016-3956.

[69] Paredes, P., Choudhari, M., and Li, F., "Transition due to streamwise streaks in a supersonic flat plate boundary layer," *Physical Review Fluids*, Vol. 1, No. 8, 2016, pp. 083601–1–23. doi:10.1103/PhysRevFluids.1.083601.

[70] Paredes, P., Choudhari, M., and Li, F., "Transient growth and streak instabilities on a hypersonic blunt body," AIAA Paper 2017-0066, 2017. doi:10.2514/6.2017-0066.

[71] Paredes, P., Choudhari, M., Li, F., Jewell, J., Kimmel, R., and Marineau, E., "Nonmodal growth of traveling waves on blunt cones at hypersonic speeds," *Physical Review Fluids*, 2018, (in preparation).

[72] Xie, Z., Karimi, M., and Girimaji, S., "Small perturbation evolution in compressible Poiseuille flow: pressure-velocity interactions and obliqueness effects," *Journal of Fluid Mechanics*, Vol. 814, 2017, pp. 249–276. doi:10.1017/jfm.2016.795.

[73] Orr, W., "The stability or instability of the steady motions of a perfect liquid and of a viscous liquid. Part I: A perfect liquid," *Proceedings of the Royal Irish Academy A*, Vol. 27, 1907, pp. 9–68. URL http://www.jstor.org/stable/20490590.

[74] Orr, W., "The stability or instability of the steady motions of a perfect liquid and of a viscous liquid. Part II: A viscous liquid," *Proceedings of the Royal Irish Academy A*, Vol. 27, 1907, pp. 69–138. URL http://www.jstor.org/stable/20490591.

[75] Butler, K., and Farrell, B., "Three-dimensional optimal perturbations in viscous shear flow," *Physics of Fluids*, Vol. 4, No. 8, 1992, pp. 1637–1650. doi:10.1063/1.858386.